# charged pion multiplicaties in SIDIS with 10.6 GeV electrons 2 P. Bosted, H. Bhatt, S. Jia, W. Armstrong, D. Dutta, R. Ent, D. Gaskell, 3 E. Kinney, H. Mkrtchyan, S. Ali, R. Ambrose, D. Androic, C. Averbe Gayoso,<sup>2</sup> A. Bandari,<sup>1</sup> V. Berdnikov,<sup>8</sup> D. Bhetuwal,<sup>2</sup> D. Biswas,<sup>11</sup> M. Boer,<sup>3</sup> E. Brash, <sup>12</sup> A. Camsonne, <sup>5</sup> M. Cardona, <sup>3</sup> J. P. Chen, <sup>5</sup> J. Chen, <sup>1</sup> M. Chen, <sup>13</sup> E. M. Christy, <sup>11</sup> S. Covrig, <sup>5</sup> S. Danagoulian, <sup>14</sup> M. Diefenthaler, <sup>5</sup> B. Duran, <sup>3</sup> C. Elliot, <sup>15</sup> H. Fenker, <sup>5</sup> E. Fuchey, <sup>16</sup> J. O. Hansen, <sup>5</sup> F. Hauenstein, <sup>17</sup> T. Horn, <sup>8</sup> G. M. Huber, M. K. Jones, M. L. Kabir, A. Karki, B. Karki, S. J. D. Kay, 9, 19 C. Keppel,<sup>5</sup> V. Kumar,<sup>9</sup> N. Lashley-Colthirst,<sup>11</sup> W. B. Li,<sup>1,2</sup> D. Mack,<sup>5</sup> S. Malace,<sup>5</sup> 10 P. Markowitz, <sup>20</sup> M. McCaughan, <sup>5</sup> E. McClellan, <sup>5</sup> D. Meekins, <sup>5</sup> R. Michaels, <sup>5</sup> 11 A. Mkrtchyan, G. Niculescu, I. Niculescu, B. Pandey, 11, 22 S. Park, E. Pooser, 5 12 B. Sawatzky, <sup>5</sup> G. R. Smith, <sup>5</sup> H. Szumila-Vance, <sup>5,20</sup> A. S. Tadepalli, <sup>5</sup> V. Tadevosyan, <sup>7</sup> 13 R. Trotta, <sup>8</sup> H. Voskanyan, <sup>7</sup> S. A. Wood, <sup>5</sup> Z. Ye, <sup>4,24</sup> C. Yero, <sup>20</sup> and X. Zheng <sup>13</sup> 14 (for the Hall C SIDIS Collaboration) 15 <sup>1</sup> The College of William & Mary, Williamsburg, Virginia 23185, USA 16 <sup>2</sup> Mississippi State University, Mississippi State, Mississippi 39762, USA 17 <sup>3</sup> Temple University, Philadelphia, Pennsylvania 19122, USA 18 <sup>4</sup>Argonne National Laboratory, Lemont, Illinois 60439, USA 19 <sup>5</sup> Thomas Jefferson National Accelerator Facility, Newport News, Virginia 23606, USA 20 <sup>6</sup>University of Colorado Boulder, Boulder, Colorado 80309, USA 21 <sup>7</sup>A.I. Alikhanyan National Science Laboratory, 22 Yerevan Physics Institute, Yerevan 0036, Armenia <sup>8</sup>Catholic University of America, Washington, DC 20064, USA <sup>9</sup> University of Regina, Regina, Saskatchewan S4S 0A2, Canada 25

Flavor, transverse momentum and azimuthal dependence of

1

26

28

29

30

University of Virginia, Charlottesville, Virginia 22903, USA
 North Carolina A & T State University, Greensboro, North Carolina 27411, USA

<sup>10</sup> University of Zagreb, Zagreb, Croatia

<sup>11</sup>Hampton University, Hampton, Virginia 23669, USA

<sup>12</sup>Christopher Newport University, Newport News, Virginia 23606, USA

<sup>15</sup> University of Tennessee, Knoxville, Tennessee 37996, USA
 <sup>16</sup> University of Connecticut, Storrs, Connecticut 06269, USA
 <sup>17</sup> Old Dominion University, Norfolk, Virginia 23529, USA
 <sup>18</sup> Ohio University, Athens, Ohio 45701, USA
 <sup>19</sup> University of York, Heslington, York, Y010 5DD, UK
 <sup>20</sup> Florida International University, University Park, Florida 33199, USA
 <sup>21</sup> James Madison University, Harrisonburg, Virginia 22807, USA
 <sup>22</sup> Virginia Military Institute, Lexington, Virginia 24450, USA
 <sup>23</sup> Stony Brook University, Stony Brook, New York 11794, USA
 <sup>24</sup> Tsinghua University, Beijing 100084, China
 (Dated: July 21, 2025)

31

32

33

34

35

36

37

38

39

40

41

42

Abstract

Measurements of SIDIS multiplicities for  $\pi^+$  and  $\pi^-$  from proton and deuteron targets are 43 reported on a grid of hadron kinematic variables  $z, P_T$ , and  $\phi^*$  for leptonic kinematic variables 44 0.3 < x < 0.6 and  $3 < Q^2 < 5~{\rm GeV^2}.$  Data were acquired in 2018 at Jefferson Lab Hall C 45 with a 10.6 GeV electron beam impinging on 10-cm-long liquid hydrogen and deuterium targets. 46 Scattered electrons were detected in the HMS spectrometer, and pions were detected in the SHMS spectrometer. The multiplicities were fitted for each bin in  $(x, Q^2, z, P_t)$  with three parameters:  $\phi^*$  independent  $M_0$  and azimuthal modulations  $2\langle\cos(\phi^*)\rangle$  and  $2\langle\cos(2\phi^*)\rangle$ . The  $P_t$ -dependence 49 of the  $M_0$  results was found to be remarkably independent of  $P_t$  for the four flavor cases studied:  $ep \to e\pi^+ X$ ,  $ep \to e\pi^- X$ ,  $ed \to e\pi^+ X$ ,  $ed \to e\pi^- X$  over the range  $0 < P_t < 0.4$  GeV. A single Gaussian fit to the  $P_t$  dependence gives a poor description. A fit to previous world data using a 52 Gaussian plus a weighted Gaussian provides considerable improvement. The  $P_t$  distributions were 53 found to increase slowly with z. The  $\cos(\phi^*)$  modulations were found to be consistent with zero 54 for  $\pi^+$  and greater than zero for  $\pi^-$ , in strong contrast to the dominance predicted by the "Cahn 55 effect", but in agreement with previous world data. The  $\cos(2\phi^*)$  modulations were found to be consistent with zero.

### 58 I. INTRODUCTION

Over the last five decades, semi-inclusive deep-inelastic (SIDIS) lepton-nucleon scattering 59  $(lN \to l'hX)$  has proven to be a key tool in building a more complete and accurate picture of the internal structure of the nucleon in terms of the partonic degrees of freedom of quantum 61 chromodynamics (QCD). It has been instrumental in establishing that the collinear picture 62 of the quark-parton model is incomplete. One of the most important advantages of SIDIS is 63 the ability to measure the yield of hadrons (h) both in terms of the longitudinal momentum fraction z and the transverse momentum  $P_t$  (shown schematically in Fig. 1). The SIDIS 65 process in its simplest interpretation can be thought of as a subset of deep-inelastic scattering (DIS), described by parton distribution functions (PDFs), with a multiplicity function (M) that indicates the probability of the DIS final state containing a particular meson with a particular momentum vector. In this highly simplified picture, the multiplicity dependence on  $P_t$  arises from a convolution of the transverse momentum of the quark  $(k_T)$  and the transverse momentum generated in the fragmentation process  $(p_{\perp})$ , in which the struck quark 71 hadronizes into multiple final-state particles. A Comparison of SIDIS from protons (u-quark 72 dominated) and neutrons (d-quark dominated) could, in principle, be used to constrain the 73 difference between the average  $k_T$  of up and down valence quarks in the nucleon. Expanding 74 the kinematic coverage for both positive and negative pions can help to distinguish differences 75 in "favored" and "unfavored" fragmentation functions, where "favored" refers to a pion 76 containing the struck quark. The azimuthal modulations of the measured pion relative to 77 the virtual photon direction are also sensitive to  $k_T$ , especially when the incident electron 78 or target nucleon are polarized. [1, 2] 79

In this paper, we present the results of a dedicated spectrometer experiment at Jefferson Lab, designed to augment the global SIDIS data set through high precision measurements from both hydrogen and deuteron targets, with measurements of both positively and negatively charged pions in the kinematic region accessible with an 10.6 GeV electron beam and in-plane spectrometers. The high luminosity of this experiment has permitted binning the multiplicity results in a fine 3-dimensional grid in z,  $P_t$ , and azimuthal angle  $\phi^*$ . Neither the beam nor the target was polarized for this experiment. However, our results provide a crucial benchmark for the interpretation of SIDIS experiments with polarization degrees of freedom.

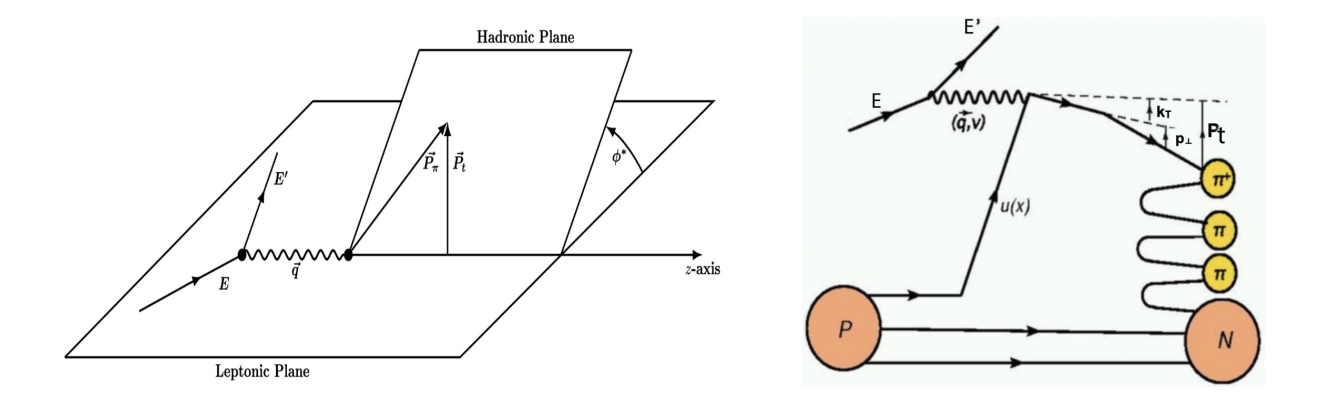


FIG. 1. (left) Kinematics of the SIDIS process in the  $\gamma^*P$  center of mass frame. (right) Simplified schematic of the pion SIDIS process, showing that the final transverse momentum of the leading pion,  $P_t$ , arises from the convolution of the struck quark's transverse momentum,  $k_T$ , with the transverse momentum generated during the fragmentation,  $p_{\perp}$ .

### A. Formalism

The semi-inclusive scattering of unpolarized electrons by unpolarized nucleons in the SIDIS kinematic region can be described formally [3] in terms of structure functions (SF) as

$$\frac{d\sigma}{dx \, dy \, d\psi \, dz \, d\phi^* \, dP_t^2} = \frac{\alpha^2}{xyQ^2} \frac{y^2}{2(1-\epsilon)} (1 + \frac{\gamma^2}{2x})$$

$$\left\{ F_{UU,T} + \epsilon F_{UU,L} + \sqrt{2\epsilon(1+\epsilon)} \cos(\phi^*) F_{UU}^{\cos(\phi^*)} + \epsilon \cos(2\phi^*) F_{UU}^{\cos(2\phi^*)} \right\}$$
(1)

The four SF  $(F_{UU,T}, F_{UU,L}, F_{UU}^{\cos(\phi^*)}, \text{ and } F_{UU}^{\cos(2\phi^*)})$  are all functions of  $(x, Q^2, z, P_t)$ , where  $(x, Q^2, y)$  are the standard DIS virtual photon variables,  $\epsilon$  is the virtual photon polarization, and the detected hadron is characterized by its momentum fraction z, transverse momentum  $P_t$ , and azimuthal angle  $\phi^*$  of the hadronic reaction plane relative to the plane defined by the incident and scattered electron. We use the "Trento" convention for the definition of  $\phi^*$  [3]. The fine structure constant is represented by  $\alpha$ , the kinematic factor  $\gamma = 2Mx/Q$ , where M is the nucleon mass. We define multiplicities as the ratio of the SIDIS cross section (Eq. 1) to the DIS cross section calculated as a function of  $(x, Q^2, y, \epsilon)$ .

# B. Theoretical interpretation

100

Significant advances were made in incorporating  $\vec{k}_T$  into the theoretical description of 101 SIDIS processes. For example, the transverse momentum dependent (TMD) parton distri-102 bution functions (PDF) and fragmentation functions (FF) [4, 5] were introduced, and a TMD 103 factorization formalism [6] was developed. The factorization framework demonstrates that 104 the hadron transverse momentum arises from the transverse momentum of the quarks in the 105 nucleon, combined with the transverse momentum generated during quark fragmentation. 106 Both the TMD and the FF depend on two independent variables: the TMD on x and  $k_T$ , 107 while the FF depends on z and the transverse momentum  $p_{\perp}$  of the hadron acquired dur-108 ing the fragmentation process. The TMD factorization was first shown for the high-energy 109 limit (high values of the virtuality scale,  $Q^2 >> \Lambda_{\rm QCD}$ ) and moderate values of  $P_t \sim \Lambda_{\rm QCD}$ . 110 However, its applicability at moderate  $Q^2$  has since been observed in several experiments [7– 111 10]. Within this framework, and with the approximation that higher-order (higher-twist) 112 corrections are suppressed by powers of 1/Q, the SIDIS differential cross section is given by 113 18 structure functions that are convolutions of various TMD PDF and FF [3]. This large 114 number of structure functions is a consequence of the fact that, for a spin-1/2 hadron, there 115 are 8 TMD [3, 4, 11], each representing a unique correlation between the spin and the orbital 116 motion of the partons. These TMD are parameterized using the world data on SIDIS and 117 other processes [12–16]. 118

As expected, the unpolarized SIDIS cross section can only provide information about the 119 unpolarized TMD distribution functions and the unpolarized TMD fragmentation functions. 120 The  $\cos(\phi^*)$  dependence was predicted in 1978 by R. Cahn [17] as a result of the interaction 121 of the virtual photon with quarks in the nucleon possessing intrinsic transverse momentum. 122 Both the  $\cos(\phi^*)$  and  $\cos(2\phi^*)$  modulations receive contributions from the Boer-Mulders 123 effect [18], arising from a correlation between the quark's intrinsic transverse momentum 124 and its transverse spin, coupled to the Collins fragmentation function [19], which preserves 125 the correlation with fragmentation dependent on the struck quark's transverse spin. Phe-126 nomenological analyses by Barone et al. [15] stress that these structure functions are sen-127 sitive to higher-twist contributions. Additionally, the transverse momentum dependence of 128 the TMD and FF are expected to be approximately Gaussian [1], for low values of  $P_t$ . To 129 leading order, this simplification and momentum conservation give:  $\langle \vec{P}_t^2 \rangle \simeq \langle \vec{p}_\perp^2 \rangle + z^2 \langle \vec{k}_T^2 \rangle$ , 130

implying that the transverse momentum dependence of TMD and FF can be parameterized by a normalized linear combination of a Gaussian and a  $z^2$ -weighted Gaussian [16].

## C. Previous experiments

133

Some of the earliest SIDIS experimental studies in the valence quark region (x > 0.25)134 were made at Cornell in the 1970s, using 12 GeV electrons [20]. These experiments demon-135 strated that multiplicities behave roughly as  $(1-z)^2$  for z<0.7, have an approximately 136 Gaussian distribution in  $P_t$ , and have relatively small dependence on  $\phi^*$  compared to exclusive pion electroproduction. Subsequent experiments [7, 9, 21–23] showed that spin-averaged 138 cross sections can be described as a convolution of quark PDFs derived from DIS and Drell-139 Yen reactions with FF derived from electron-positron colliders. They also demonstrated 140 the usefulness of describing the production of leading meson that contains the struck quark 141 flavor with "favored" FF, while other mesons are described by "unfavored" FF, which ex-142 hibit a smaller strength at high z than favored FF. An experiment at Jefferson Lab Hall 143 C with 6 GeV electrons [7] showed a duality between the results in the resonance region, 144 at low center-of-mass energy (2 < W < 3 GeV), and the results well above the nucleon 145 resonance region (W > 3 GeV). This was true as long as the electron-pion invariant missing 146 mass squared,  $M_x^2$ , was well above 2.5 GeV<sup>2</sup> (corresponding to z < 0.7 at these kinematic 147 settings), as shown in Fig. 2. The noticeable peak centered at  $M_x^2 = 1.5 \text{ GeV}^2$ , visible in this 148 figure was due to the semi-exclusive channel  $ep \to e\pi\Delta(1232)$ , which was not subtracted in 149 that analysis (but is subtracted in the present analysis). Simple phenomenological fits [8, 10] 150 to these data attempted to disentangle the up and down valence quark  $k_T$  widths, as well 151 as favored and unfavored FF widths, with the assumptions that the  $\cos \phi^*$  dependence is 152 dominated by the Cahn term and that the fragmentation widths are independent of z (both 153 of which have since been shown to be incorrect). 154

The experimental results prior to 2018 cannot be considered conclusive due to the limited kinematic coverage, low counting rates, inadequate particle identification, and poor resolution in  $\phi^*$  at low  $P_T$ . In order to overcome many of these limitations, a new experimental program was initiated at the energy-upgraded Jefferson Lab, using both the wide-acceptance, lower luminosity CLAS12 detector in Hall B and the high-luminosity, small acceptance spectrometers in Hall C. The broad program includes the use of beam and target polarization,

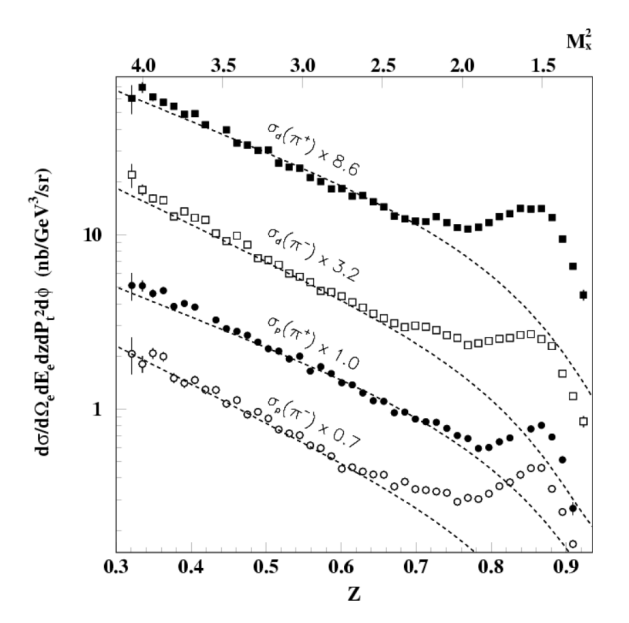


FIG. 2. SIDIS cross sections for charged pions from proton and deuteron targets from Ref. [7] with 5.6 GeV electrons at Jefferson Lab Hall C as a function of z and corresponding electron-pion missing mass squared  $M_x^2$ .

both light and heavy nuclear targets, a range of electron beam energies, and identification of many final state mesons. In this paper, we report on spectrometer results for charged pions with an unpolarized beam and target at the highest available beam energy, from an experiment [24] that was an integral part of the JLab SIDIS program and was completed in 2019. The experiment featured a wide range of  $(x, Q^2)$  values (to study higher-twist contributions), full  $\phi^*$  coverage for  $P_T < 0.25$  GeV, a larger  $P_T$  range for  $\phi^*$  near 180°, and a broad range in z (to help distinguish  $k_T$  width from  $p_{\perp}$  widths).

# 8 II. THE EXPERIMENT

The experiment was carried out in spring 2018 and fall 2019, in Hall C at Jefferson Lab (JLab). Electrons scattered from hydrogen and deuterium cryogenic targets were detected in the High Momentum Spectrometer (HMS), with alternatively positive and negative pions detected in the Super High Momentum Spectrometer (SHMS). An overview of the experiment layout is shown in Fig. 3.

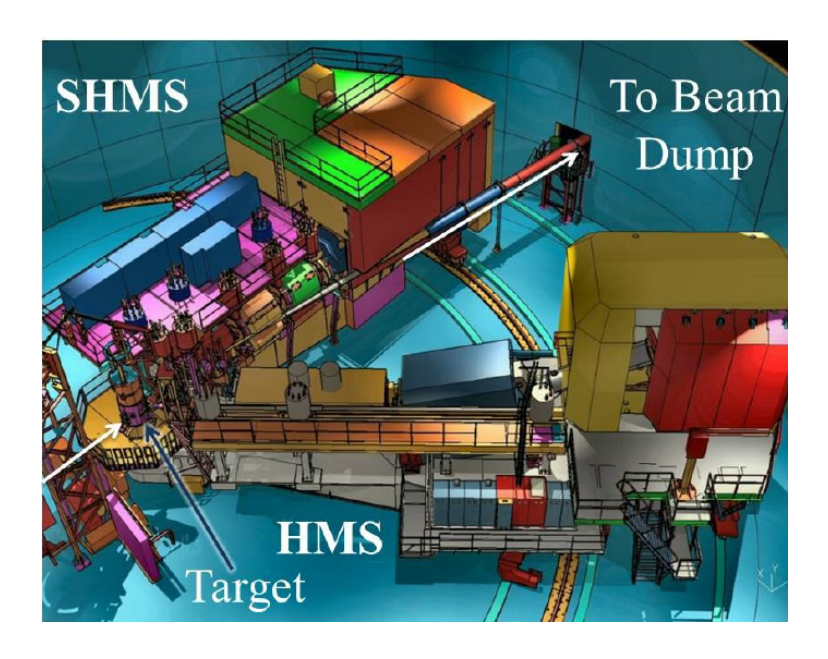


FIG. 3. Overview of the experimental setup in Hall C at JLab.

#### A. Electron beam

174

The experiment used a quasi-continuous wave electron beam with beam energy of 175 10.6 GeV and beam currents ranging from 2  $\mu$ A to 70  $\mu$ A. The spacing of the beam 176 micro-bunches was 4 ns for this experiment. To minimize density reduction in the target 177 due to the formation of bubbles from localized beam heating, the beam was rastered over 178 a  $2\times2$  mm<sup>2</sup> square pattern at  $\approx25$  kHz. The beam energy was determined by measuring 179 the bend angle of the beam on its way into Hall C as it traversed a set of magnets with 180 precisely known field integrals. The relative uncertainty of the beam energy was <0.05%. A 181 set of resonant-cavity-based beam-current monitors (BCM) was used to determine the total 182 accumulated beam charge, and a parametric transformer was used to monitor the gain of the 183 BCMs. The inclusive electron scattering rate from a carbon foil was monitored to determine 184 a small correction to the measured beam current by enforcing the current independence of 185 the inclusive rate. After correcting for zero-offsets and saturation effects measured using a 186 solid carbon target, the relative uncertainty of the accumulated beam charge was  $\approx 0.5\%$ . 187

# B. Targets

188

The two main production targets were liquid hydrogen and liquid deuterium, each cir-189 culated through 10 cm long and 3.4 cm radius aluminum cylinders with side thicknesses of 190 0.2 mm and front (exit) end-cap thicknesses of 0.14 mm (0.19 mm). At the pressure and 191 temperature used in the experiment, the nominal areal density of the  $LH_2$  was  $714\pm14$ 192  $mg/cm^2$  for kinematic settings I and III, and  $718 \pm 8$   $mg/cm^2$  for kinematic setting II (the 193 kinematic settings are listed in Table I). The nominal areal density of the  $LD_2$  was  $1662 \pm 33$ 194  $\rm mg/cm^2$  for kinematic settings I and III, and  $1662 \pm 17 \rm mg/cm^2$  for kinematic setting II. 195 A small reduction in the nominal density of the cryogenic targets due to beam heating was 196 measured to be  $-0.023\%/\mu A$ . A so-called "dummy target" consisting of two aluminum foils each with an areal density of 181 mg/cm<sup>2</sup> placed 10 cm apart was used to measure the 198 contribution from the entrance and exit end-caps of the cryogenic target cells. The targets 199 were cycled every few hours, reducing the systematic errors on the ratio of multiplicities 200 from hydrogen and deuterium, compared to experiments in which targets are changed on a 201 much longer time frame. 202

# C. Kinematics

203

213

214

The angle and momentum of the electron arm (13<  $\theta_e$  <20°, 3< E' <5.2 GeV) and the hadron arm (6<  $\theta_{\pi}$  <30°, 2<  $P_{\pi}$  <6 GeV) were chosen to map a region in x and z between 0.25-0.65 and 0.3-0.7, respectively. The spectrometers are constrained to rotate around the target in a horizontal plane, which limits the out-of-plane angular coverage to about 0.08 radians. The angle,  $\theta_{pq}$ , between the electron three-momentum transfer,  $\vec{q}$ , and the hadron momentum, was chosen to cover a range in  $P_T$  up to 0.8 GeV. The electron kinematic settings of the experiment are listed in Table I, along with the range of pion momenta and angles covered at each setting.

D. Electron Identification

Scattered electrons were detected on the well-studied High Momentum Spectrometer [25], in use since 1996. As shown in Fig. 4, the detector package includes two pairs segmented

TABLE I. Beam energy E, HMS momentum E', HMS angle  $\theta_e$ , corresponding values of DIS variables x,  $Q^2$ , and W, and SHMS range of central momentum  $(p_{\pi})$  and angle  $(\theta_{\pi})$  settings.

Setting	Е	E'	$\theta_e$	$Q^2$	W	x	$p_{\pi}$	$ heta_\pi$
	(GeV)	(GeV)	(deg)	$(\mathrm{GeV}^2)$	(GeV)		(GeV)	(deg)
I	10.6	5.240	13.50	3.1	2.8	0.31	2.4 - 4.9	6.5 - 30
II	10.6	3.307	19.70	4.1	3.3	0.30	2.6 - 6.6	6.5 - 22
III	10.6	5.240	16.30	4.5	2.6	0.45	2.0 - 4.8	8 - 30

planes of plastic scintillators used to determine the time of arrival of particles transported through the spectrometer magnets, with a time resolution of about 0.3 ns. The planes were grouped into pairs (x, y) separated by 2 m, allowing the particle speed to be determined with a resolution of about 0.1 in  $\beta$ .

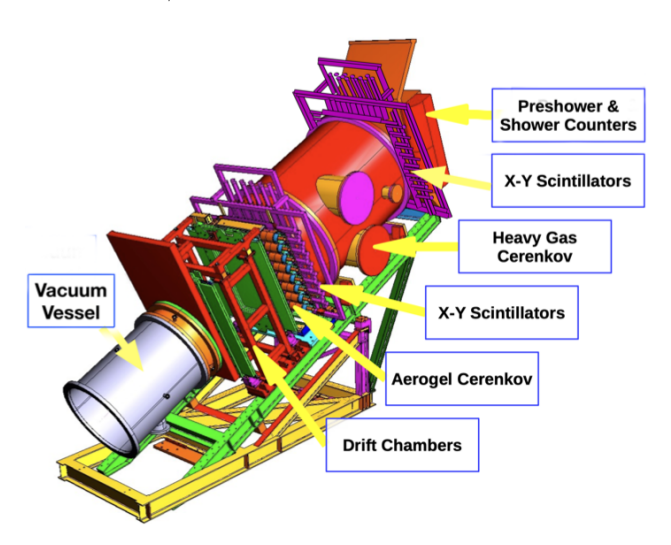


FIG. 4. Detector configuration in the HMS

221

222

223

225

226

227

Two drift chambers, each containing six planes of wires oriented at 0° and  $\pm 60$ ° with respect to horizontal, provided position and direction (track) information at the spectrometer focal plane with a resolution of <250  $\mu$ m. Only tracks whose projected positions at the locations of the other detectors and the spectrometer vacuum pipe were within fiducial volumes were kept. The track information was then used to reconstruct the momentum and angle of the particle at the target. Only tracks within a fiducial volume in relative momentum ( $-9 < \delta P/P < 11\%$ ), in-plane relative angle ( $-30 < \theta_y < 30$  mr) and relative out-of-plane angle ( $-65 < \theta_x < 65$  mr) were kept. If multiple tracks were found, a track

"pruning" algorithm was used to determine which track was actually associated with the time and position at the scintillator planes and the calorimeter. The tracking efficiency in the HMS was over 99.7% for the entire experiment.

A two-mirror threshold gas Cherenkov detector and a segmented Pb-glass calorimeter [26] were used to distinguish electrons from pions (both of which generally passed the cut on scintillator paddle timing). The Cherenkov detector gas mixture and pressure were set to give a pion threshold of 4.5 GeV. The average number of photo-electrons (p.e.) produced by electrons was about 6 (10) in the upper (lower) mirrors for settings I and II, due to a crack in the upper mirror. With a threshold of 0.3 p.e., the electron detection efficiency was determined to be > 99.5%. For setting III, the cracked mirror was fixed, resulting in an average of 10 photoelectrons from each mirror. A light leak resulted in very high counting rates, which effectively blocked some of the electron signals from being read out. Using a threshold of 1 p.e. to reduce this effect, we determined an effective average efficiency of 0.975 for electrons, independent of beam current.

Scattered electrons were identified in the segmented lead glass electromagnetic calorimeter using the ratio of energy deposited in the blocks near the projected track position  $(E_{cal})$  to the track momentum  $(P_e)$ . As illustrated in Fig. 5, the  $E_{cal}/P_e$  distributions for each of the three kinematic settings show a narrow peak centered on unity. The small flat-looking distributions below 0.75 are mostly from pions. The vertical dashed line at 0.75 shows the cut used for electron identification. The electron detection efficiency of the HMS calorimeter was greater than 99.7%. After correcting for accidental coincidences, the contamination of pions in the final event sample was less than 0.5%.

### E. Pion Identification

Charged pions were detected in the Super High Momentum Spectrometer [27], used for the first time in 2018. Considerable effort was made prior to the present experiment to understand its optical properties and acceptance, as well as to commission all of the detectors. The momentum and angle ranges used at each kinematic setting are listed in Table I, and were chosen to provide good coverage in the region 0.3 < z < 0.7, along with as much coverage in  $P_t$  and  $\phi^*$  as allowed by the spectrometer constraints. The polarity of the spectrometer was alternated every few days in order to separately accumulate positively

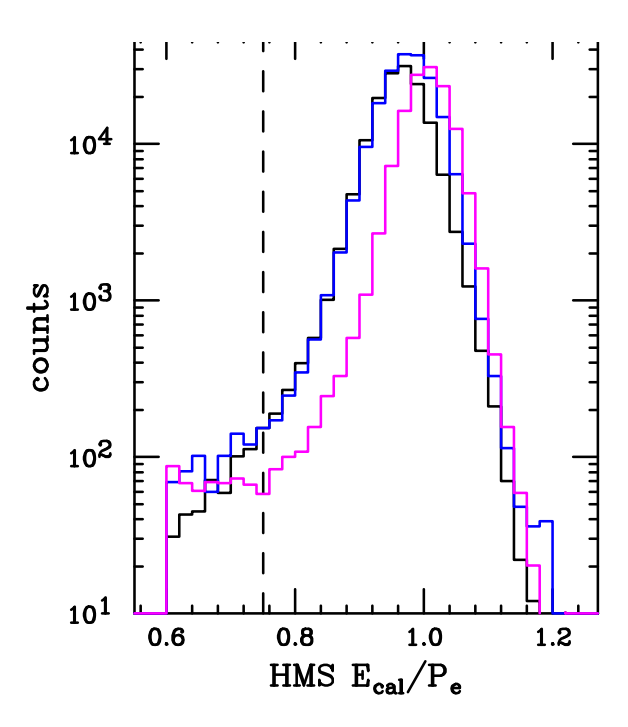


FIG. 5. Accidental-subtracted distributions of normalized HMS calorimeter energy  $(E_{cal}/p_e)$  for kinematic setting I (black), II (blue), and III (magenta), for electron-pion coincidence events passing all cuts except the  $E_{cal}/p_e > 0.75$  cut, which is indicated by the vertical dashed line.

and negatively charged pions. This technique provides identical acceptance for both charge states, resulting in small systematic errors in the ratios of multiplicities, compared to large acceptance devices such as CLAS [28, 29].

As in the HMS, the SHMS detector configuration (see Fig. 6) included two pairs of segmented planes of scintillators separated by 2 m to give fast timing signals and rough particle trajectories. The resolution in particle speed was sufficient to reject protons with momenta below 2 GeV. The average arrival time in the four paddles was compared to the arrival time of the 4 ns spaced beam micro-bunches. With a flight path of about 22 m in the SHMS spectrometer, and a relative timing cut of  $\pm 0.7$  ns , it was possible to remove all protons and most kaons from the event sample, as illustrated in Fig. 7. The efficiency of the timing cut was about 96% for setting III. The RF timing signal was not operational for Settings I and II.

Two drift chambers, similar to those in the HMS, were used for tracking. Track pruning and detector position fiducial cuts were applied in a similar manner to the HMS. Only tracks within a fiducial volume in relative momentum ( $-15 < \delta P/P < 18\%$ ), relative in-plane angle

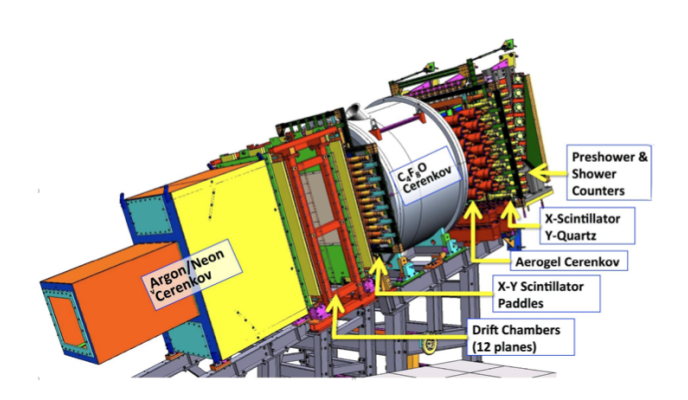


FIG. 6. Detector configuration in the SHMS

 $(-30 < \theta_y < 30 \text{ mr})$ , and relative out-of-plane angle  $(-55 < \theta_x < 55 \text{ mr})$  were kept. The tracking efficiency was found to drop from about 99.5% at low rates to about 97% at the highest rates of particles entering the detector hut. To avoid pile-up effects in the tracking, we kept the particle rate below 700 kHz by lowering the beam current to values as low as 2  $\mu A$ .

To separate pions from electrons (or positrons), kaons, and protons, three detectors were 279 used: an aerogel Cherenkov detector, a heavy gas Cherenkov detector, and an electromag-280 netic lead-glass calorimeter. The aerogel detector was outfitted with multiple blocks with 281 an index of refraction of 1.015, corresponding to Cherenkov light thresholds of 0.9, 2.85, 282 and 5.4 GeV for pions, kaons, and protons, respectively. Above threshold, an average of 10 283 p.e. was produced. Below the Cherenkov threshold, kaons and protons often produced a few 284 p.e. through knock-on scattering, as shown in Fig. 7. We therefore required a minimum of 285 4 p.e. for pion identification, with a corresponding efficiency of 95%. 286

The heavy gas Cherenkov detector contained  $C_4F_8O$  at less than 1 atm pressure, giving a pion threshold of 2.61 GeV. It has four individual mirrors to focus Cherenkov light onto photomultiplier tubes. The design resulted in a small inefficient region near the center of the detector for settings I and II, and a much larger region for setting III after an unsuccessful attempt to realign the mirrors for higher efficiency, as shown in Fig. 8. Pions with momenta above 2.85 GeV were required to have tracks outside the inefficient region and a light signal greater than 1 p.e. The efficiency of this cut varied with momentum, increasing rapidly from 96% at 2.85 GeV to 99% for  $P_{\pi} > 3.2$  GeV.

287

288

289

290

291

292

293

294

295

The segmented lead-glass, 22 radiation-length electromagnetic calorimeter was used to

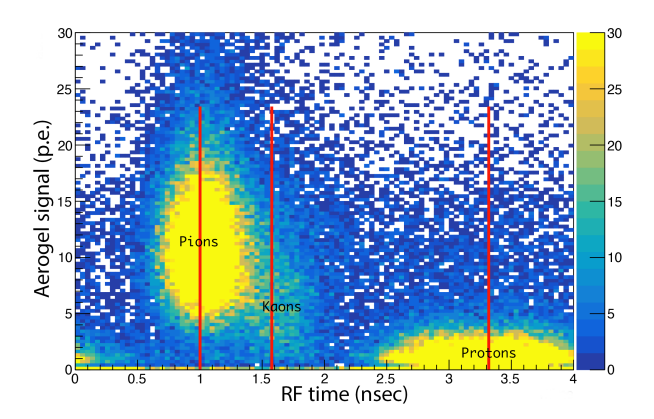


FIG. 7. SHMS aerogel signals (in p.e. ) as a function of the arrival time of arrival of pions, kaons, and protons relative to the beam micro-pulse time (RF time), modulo the 4 ns bunch spacing, for particles with momenta  $3.4 < P_{\pi} < 4.3$  GeV. The pion peak was adjusted to be a 1 ns . The red vertical lines show the location of the pion, kaon, and proton peaks.

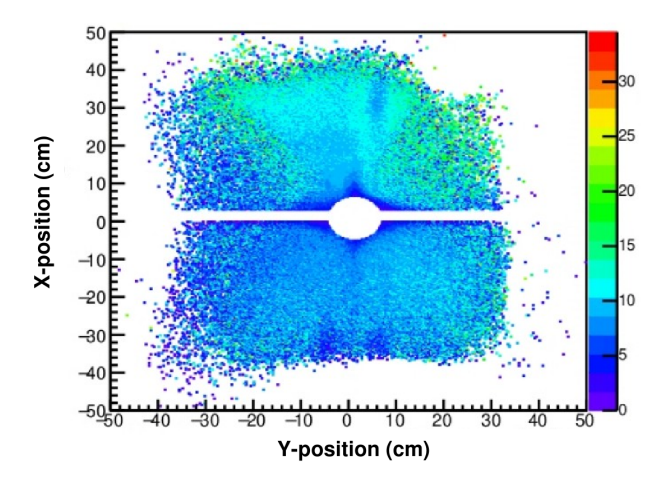


FIG. 8. The x-position vs. y-position of hits on the heavy gas Cherenkov detector, showing the inefficient region that was excluded from the analysis. The color bar represents the number of photo-electrons.

separate hadrons from electrons. In contrast to the HMS, where electrons produced a narrow peak in  $E_{cal}/P_e$  centered on unity, hadrons in the SHMS generally produced much less visible energy, as seen in the  $E_{cal}/P_{\pi}$  distribution, because the calorimeter is only about one hadronic interaction length in thickness. The distributions in  $E_{cal}/P_{\pi}$  are shown for both positive (top panel) and negative polarity (bottom panel) in Fig. 9, for good pion candidates selected by all cuts except that on  $E_{cal}/P_{\pi}$ . A peak near unity can be seen in the negative

polarity distribution, which we ascribe to accidental electron-electron coincidences. The peak is largely suppressed when accidental coincidences are removed (blue curves). There is essentially no evidence of electron-positron coincidences in the positive polarity distributions. The residual distributions for  $E_{cal}/P_{\pi} > 0.8$  are likely dominated by charged-to-neutral pion conversions at the start of the hadronic shower process. Nonetheless, we imposed a cut  $E_{cal}/P_{\pi} < 0.8$  to ensure no electron or positron contamination of the pion signal, with a typical efficiency of 0.94-0.97, depending on the spectrometer momentum.

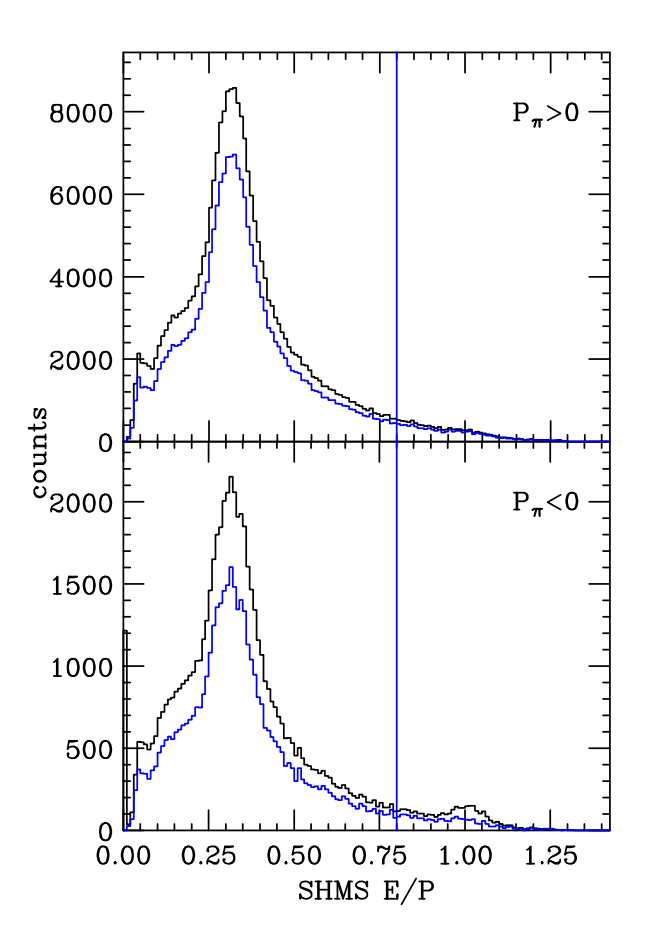


FIG. 9. Distributions of  $E_{cal}/P_{\pi}$  in the SHMS calorimeter for positive (top panel) and negative (bottom panel) pion candidates. The blue curves represent subsets of the black distributions with accidental coincidences subtracted. The vertical line at 0.8 indicates the cut used to reject positrons (top panel) and electrons (bottom panel).

The Noble gas Cherenkov detector was installed only for settings I and II. With a pion threshold of over 5 GeV, it was not directly used for pion identification. Its main use was to provide a clean sample of electrons for calibrating the calorimeter. Additional information

on the detectors used in the experiment, plots of the trigger efficiency and the detector efficiencies can be found in Ref. [30–32].

# F. Electron-pion coincidence identification

At the high luminosity of Hall C, there were many triggers for which an electron and a pion originate from different beam bunches, spaced by 4 ns for this experiment. Fig. 10 shows the electron-pion time difference distribution for a typical kinematic setting. The green lines indicate the region used to define the in-time coincidences, while the four sets of blue lines represent accidental coincidence regions-two on each side of the main peak. The

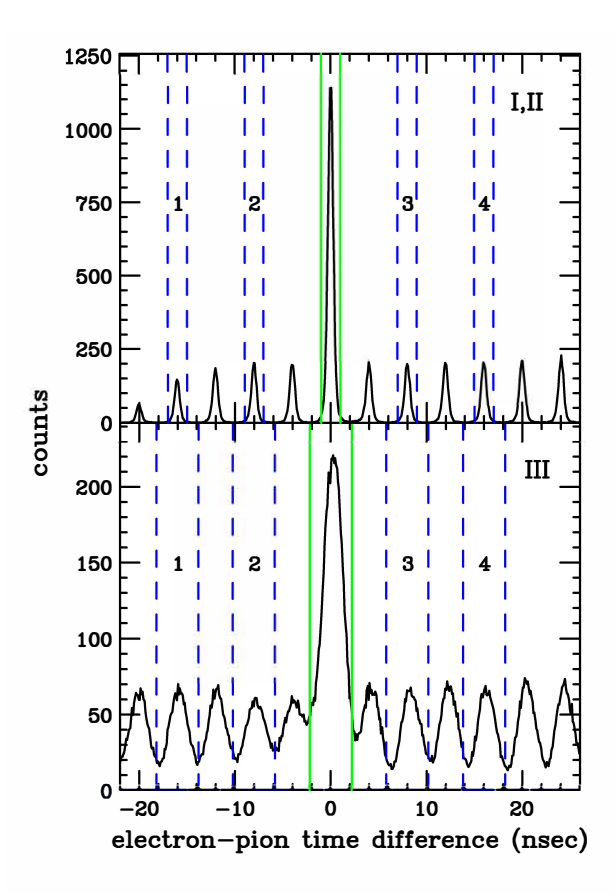


FIG. 10. Distribution of electron-pion time distributions for settings I and II (top panel) and setting III (bottom panel). The green vertical lines show the cuts used for true coincidences, with the four pairs of blue dashed lines showing the four regions used for accidental subtraction.

average number of events in these four accidental peaks was subtracted from the main peak to select true electron-pion coincidences. For settings I and II (Spring 2018), the peak width

was about 0.4 ns, consistent with the expected time resolution of the trigger scintillators in both spectrometers, and a cut of  $\pm 1$  ns was used to identify in-time coincidences. For setting III (Fall 2018), a mis-cabling problem caused the peak to be much wider (2.2 ns), reducing the ability to reject kaons and protons using coincidence timing. A wider cut of  $\pm 2$  ns was therefore applied for setting III. Fortunately, the RF timing was operational for setting III, which more than compensated for this deficiency. The accidental-to-real ratio varied throughout the experiment from 10% to 50%.

# G. Readout Trigger and Data acquisition

331

The trigger consisted of in-time signals on any three out of the four hodoscope planes in 332 each spectrometer. This ensured essentially 100% trigger efficiency. The time resolution of 333 each plane was about 0.5 ns, resulting in an accuracy of typically 0.3 ns for the electron-pion 334 time difference. The trigger signaled the Data Acquisition (DAQ) system [33] to read out 335 pulse time and height information for all the detectors in both spectrometers, and record 336 them at rates of up to 3000 Hz. In Spring 2018, a buffering system was not in place, which 337 meant that up to 40% of events were not recorded. Buffering mode was implemented for 338 Fall 2018, resulting in 100% of events being recorded. Data "runs" typically lasted about 339 one hour. 340

During the Spring 2018 runs (settings I and II), several problems caused a rate-dependent 341 loss of information for the desired electron-pion coincidences. These included a non-optimal 342 configuration of the Flash ADC modules used to read out pulse heights, non-optimal timing 343 windows for the multi-hit TDCs, and the use of more than one trigger type, such as pre-344 scaled triggers from the HMS or SHMS only. The multiplicative correction factor  $C_{DT}$  for 345 these effects, determined by running with different beam currents under otherwise identical 346 conditions, was parameterized as:  $C_{DT} = 1.03 + 0.19(R_{HMS} + R_{SHMS})$  where  $R_{HMS}$  and 347  $R_{SHMS}$  are the trigger rates in the two spectrometers, in MHz. The factor of 1.03 at zero 348 luminosity was obtained by comparing a few measurements made at identical kinematic 349 settings during Setting I and III, under the assumption that systematic normalization errors 350 were under much better control after Spring 2018. After many improvements to the hardware 351 setup in the summer of 2018, the correction was found to be much smaller:  $C_{DT} = 1 +$ 352  $0.04(R_{HMS} + R_{SHMS}).$ 

# H. Pair-symmetric background

354

In inclusive electron scattering, an important background process occurs when the mea-355 sured electron originates from the decay of a final-state hadron, especially for low values of E'/E. Approximately equal contributions come from the Dalitz decay  $\pi^0 \to \gamma e^+e^-$  and 357 from the the dominant  $\pi^0 \to \gamma \gamma$  decay, followed by subsequent pair production from one of 358 the photons in the target or spectrometer entrance window. This so-called pair-symmetric 359 background is greatly reduced in SIDIS compared to DIS by the requirement of a coinci-360 dent pion at relatively large transverse momentum with respect to the electron beam. We 361 made a dedicated measurement of the pair-symmetric background by reversing the polarity 362 of the HMS spectrometer and detecting the scattered positrons at two settings where the 363 background was expected to be the largest. The results, tabulated in Table II, indicate that 364 the pair-symmetric background is well below 0.5%. 365

TABLE II. Ratios of SIDIS rates with positrons compared to electrons in the HMS. The momentum of the HMS was 3.6 GeV and the angle was 19 degrees. Pions were measured in the SHMS with momenta of  $\pm 2.6$  GeV and angles of 16 and 20 degrees.

$P_p(GeV)$	$\theta_p(deg)$	target	$e^+/e^-$
-2.6	16	p	$0.002 \pm 0.002$
		d	$0.004 \pm 0.002$
	20	d	$0.004 \pm 0.002$
		p	$0.004 \pm 0.004$
+2.6	20	p	$0.000 \pm 0.002$
		d	$0.002 \pm 0.001$
	16	d	$0.000 \pm 0.001$

We also measured the pair-symmetric background for all the momentum/angle settings of this experiment, by exchanging the roles of the two spectrometers. The ratios of these 450 measurements lie in the range 0 to 1%, with an average of about 0.3%.

Based on these results, we did not apply any pair-symmetric correction, but assigned a systematic uncertainty of 0.3% due to this omission.

#### 1 III. MONTE CARLO SIMULATION

A Monte Carlo (MC) simulation [34], named SIMC, was performed for each target and 372 pair of spectrometer settings primarily to model the spectrometer acceptance and evaluate 373 radiative corrections. Another important use was to model pion and kaon decays (which 374 lead to muons and pions in the SHMS detector hut, respectively). For each setting, the sim-375 ulation was used to simulate a large number of events for three distinct physics processes: 376 charged pion SIDIS itself (see Sec. III A); and the two backgrounds reactions, exclusive pion 377 production; and the semi-exclusive  $\pi\Delta(1232)$  final state arising from Bremsstrahlung radi-378 ation of either in incoming or outgoing electron. These radiative contributions were treated in the angle peaking approximation using the formalism of Mo and Tsai [35]. The simulation also includes a detailed model of the targets, and geometrical acceptance and magnetic 381 field maps of the spectrometer magnets. The MC accounted for energy loss and multiple 382 scattering in the target, vacuum windows, and detectors. Meson decays were allowed at any 383 point along the particle trajectory, with the charged decay products tracked through the 384 remainder of the spectrometer. The MC has been demonstrated to accurately reproduce 385 the performance of the Hall C spectrometers [31]. The multiplicity and cross section mod-386 els used in the simulation are described in the next three sections. The SIDIS model was 387 improved by scaling the ratio of measured yields to the MC yield and iterating this process. 388

# A. SIDIS model

380

After two iterations, the charged pion SIDIS cross section model, obtained using a global fit to our results, augmented with world data is given by:

$$\sigma_{SIDIS} = \sigma_{DIS}(x, Q^2, P_t) M_{SIDIS}(z, P_t, \phi^*, x, Q^2). \tag{2}$$

The inclusive DIS cross section  $\sigma_{DIS}(x, Q^2, \epsilon)$  is from a global fit to all world data available by the year 2020 for electrons scattering from both proton and deuteron targets. It is the most comprehensive model of the DIS cross section measured with the electron spectrometer used in this experiment, and the inclusive data collected at the kinematic settings used in this paper were found to be consistent with this model to within a few percent. The z-dependence of the multiplicity function  $M_{SIDIS}(z, P_t, \phi^*, x, Q^2)$  is given by:

$$zM_{p\pi^{+}}(z,x,Q^{2}) = (q_{u}^{2}uD_{f} + q_{u}^{2}\bar{u}D_{u} + q_{d}^{2}dD_{u} + q_{d}^{2}\bar{d}D_{f} + q_{s}^{2}sD_{u} + q_{s}^{2}\bar{s}D_{u})/\sum (q_{i})^{2}$$

$$zM_{p\pi^{-}}(z,x,Q^{2}) = (q_{u}^{2}uD_{u} + q_{u}^{2}\bar{u}D_{f} + q_{d}^{2}dD_{f} + q_{d}^{2}\bar{d}D_{u} + q_{s}^{2}sD_{u} + q_{s}^{2}\bar{s}D_{u})/\sum (q_{i})^{2}$$

$$zM_{n\pi^{+}}(z,x,Q^{2}) = (q_{u}^{2}dD_{f} + q_{u}^{2}\bar{d}D_{u} + q_{d}^{2}uD_{u} + q_{d}^{2}\bar{u}D_{f} + q_{s}^{2}sD_{u} + q_{s}^{2}\bar{s}D_{u})/\sum (q_{i})^{2}$$

$$zM_{n\pi^{-}}(z,x,Q^{2}) = (q_{u}^{2}dD_{u} + q_{u}^{2}\bar{d}D_{f} + q_{d}^{2}uD_{f} + q_{d}^{2}\bar{u}D_{u} + q_{s}^{2}sD_{u} + q_{s}^{2}\bar{s}D_{u})/\sum (q_{i})^{2}$$

$$(3)$$

where,  $M_{p/n\pi^{\pm}}(z, x, Q^2)$  are the charged pion multiplicities from the proton (p) and neutron (n),  $q_i$  are the quark charges, the quark distribution functions  $u, d, s, \bar{u}, \bar{d}, \bar{s}$  were taken from CTEQ5 [36], and the favored and unfavored fragmentation functions  $D_f$  and  $D_u$  were parameterized as:

$$D_{f/u} = p_1 \zeta^{(p_2 + p_4 s_v + p_9 W^{-1})} (1 - \zeta)^{(p_3 + p_5 s_v + p_{10} W^{-1})} (1 + p_6 \zeta + p_7 \zeta^2 + p_8 \zeta^3) (1 + p_{11} W^{-1} + p_{12} W^{-2}),$$
(4)

where,  $s_v = \ln(Q^2/2)$  and the target mass corrections were applied using

$$\zeta = z \frac{1 + \sqrt{1 - 4x^2(m_\pi^2 + P_t^2)/z^2Q^2}}{1 + \sqrt{1 + 4x^2M^2/Q^2}}$$
 (5)

The fit parameters  $p_i$  were obtained from an iterative fit to the data of this experiment, and are given in Table. III.

TABLE III. Table of parameters used for  $D_{f/u}$ .

	$p_1$	$p_2$	$p_3$	$p_4$	$p_5$	$p_6$	$p_7$	$p_8$	$p_9$	$p_{10}$	$p_{11}$	$p_{12}$
$D_f$	1.0424	-0.1714	1.8960	-0.0307	0.1636	-0.1272	-4.2093	5.0103	2.7406	-0.5778	0 3.5292	7.3910
$D_u$	0.7840	0.2369	1.4238	0.1484	0.1518	-1.2923	-1.5710	3.0305	1.1995	1.3553	2.5868	8.0666

405 406

407

397

The  $P_t$  dependence of the multiplicity functions was incorporated as:

$$M_{p/n\pi^{\pm}}(z, P_t, \phi^*, x, Q^2) = \frac{1}{2\pi} M_0(z, x, Q^2) b e^{-bP_t^2},$$
(6)

i.e., a Gaussian distribution with the parameter  $b = (0.12z^2 + 0.2)^{-1} \text{ GeV}^{-2}$ , common to all processes. Note that we do not have any azimuthal dependence in this fit, consistent with the results of the present experiment. Also note that we do not have a factorized expression: the multiplicity function depends on the electron variables  $(x, Q^2, W)$ , which we found necessary to describe the data of this experiment.

# B. Exclusive pion production model

413

414

The cross sections for exclusive charged pion electroproduction were defined as:

$$\sigma = \frac{1.359}{(s - M^2)^2} (\sigma_T + \epsilon \sigma_L + \epsilon \cos(2\phi^*) \sigma_{TT} + \sqrt{2\epsilon(1 + \epsilon)} \cos(\phi^*) \sigma_{LT})$$
 (7)

where all relevant units are in GeV, M is the average nucleon mass, and the longitudinal and transverse cross sections  $\sigma_L$ ,  $\sigma_T$ , as well as two interference terms  $\sigma_{LT}$  and  $\sigma_{TT}$  are given in terms of the pion form factor  $F_{\pi}$  by:

$$F_{\pi} = (1 + p_1 Q^2 + p_2 Q^4)^{-1}$$

$$\sigma_L = (p_3 + p_{15}/Q^2)|t|/(|t| + 0.02)^2 Q^2 F_{\pi}^2 (s^{p_{11}} + \sqrt{s^{p_{17}}}) e^{p_4|t|}$$

$$\sigma_T = p_5/Q^2 e^{p_6 Q^4}/(s^{p_{12}} + \sqrt{s^{p_{16}}}) e^{p_{14}|t|}$$

$$\sigma_{LT} = (p_7/(1 + p_{10} Q^2)) e^{p_8|t|} \sin(\theta_{cm})/s^{p_{13}}$$

$$\sigma_{TT} = (p_9/(1 + Q^2)) e^{-7.0|t|} \sin(\theta_{cm})^2$$
(8)

The parameters  $p_i$  for explusive pion production from the proton  $(ep \to e\pi^+ n)$  and the neutron  $(en \to e\pi^- p)$  are obtained from fits to world data on LT separated pion electroproduction cross sections and are shown in Table IV and V.

TABLE IV. Table of parameters used for exclusive pion electroproduction cross sections.

	$p_1$	$p_2$	$p_3$	$p_4$	$p_5$	$p_6$	$p_7$	$p_8$	$p_9$	$p_{10}$
$n_{\pi^-p}$	1.60077	-0.01523	37.08142	-4.11060	23.26192	0.00983	0.87073	-5.77115	-271.08678	0.13766
$p_{\pi^+ n}$	1.75169	0.11144	47.35877	-4.69434	1.60552	0.00800	0.44194	-2.29188	-41.67194	0.69475

TABLE V. Table of parameters used for exclusive pion electroproduction cross sections.

	$p_{11}$	$p_{12}$	$p_{13}$	$p_{14}$	$p_{15}$	$p_{16}$	$p_{17}$
$n_{\pi^-p}$	-0.00855	0.27885	-1.13212	-1.50415	-6.34766	0.55769	-0.01709
$p_{\pi^+ n}$	0.02527	-0.50178	-1.22825	-1.16878	5.75825	-1.00355	0.05055

# C. Model for $\pi\Delta$

421

We modeled the semi-exclusive reactions with  $\pi\Delta(1232)$  in the final state by simply scaling fully exclusive pion electroproduction by the effective Clebsch–Gordan coefficients

determined from a fit to the data of this experiment. The coefficients are given by:

$$(ep \to e\pi^{+}\Delta^{0})/(ep \to e\pi^{+}n) = 0.4$$
  
 $(en \to e\pi^{+}\Delta^{-})/(ep \to e\pi^{+}n) = 0.8$   
 $(ep \to e\pi^{-}\Delta^{++})/(en \to e\pi^{-}p) = 0.55$   
 $(en \to e\pi^{-}\Delta^{+})/(en \to e\pi^{-}p) = 1.0$ 

The final state missing mass was simulated using a Breit-Wigner distribution for the  $\Delta(1232)$ .

# D. Kinematic dependence of radiative corrections

424

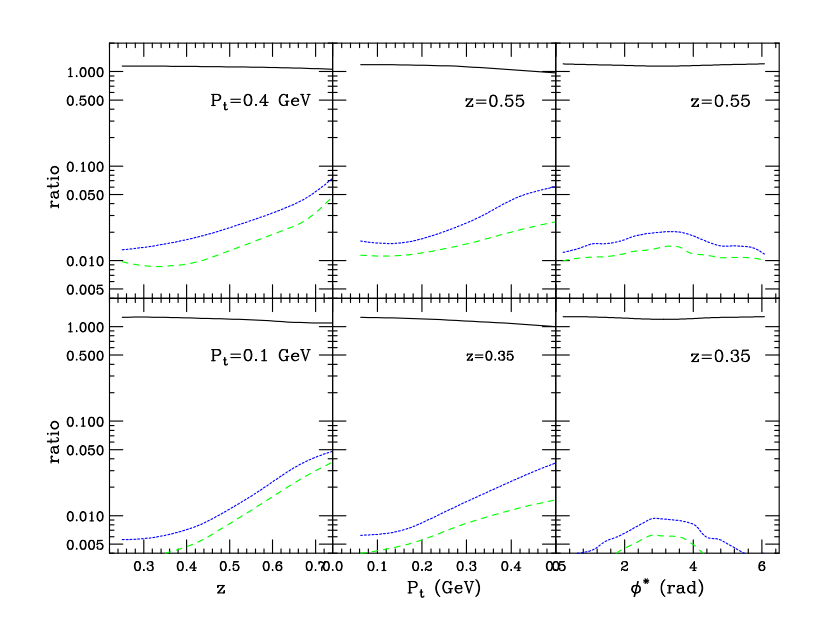


FIG. 11. The solid black curves illustrate the ratio of radiated cross sections to Born cross sections for  $\pi^+$  from a deuteron target with x=0.3 and  $Q^2=3$  GeV<sup>2</sup>. They are plotted in the left-hand panels as a function of z at  $\phi^*=180^\circ$ , for two values of  $P_t$ , in the middle panels as a function of  $P_t$  for two values of  $P_t$ , and in the right-hand panels as a function of  $P_t$  for two values of  $P_t$ , and in the right-hand panels as a function of  $P_t$  for two values of  $P_t$ . The short-dashed blue curves show the relative contribution of the radiative tail from exclusive pion production, while the long-dashed green curves show the contributions from the  $P_t$ 

The  $P_t$  dependence of the radiative corrections follows a similar pattern as the zdependence, with the overall ratio decreasing at high  $P_t$ , resulting from a strong increase of
the exclusive and  $\pi\Delta$  contributions being more than offset by a depletion of SIDIS events,
as illustrated in the middle panels of Fig. 11. The  $\phi^*$  dependence of the radiative corrections
indicates a small but non-negligible  $\cos(\phi^*)$  dependence, with the exclusive pion and  $\pi\Delta$ contributions peaking near 180°, as shown in the right-hand panels of Fig. 11.

# E. Acceptance Corrections

431

447

The predicted yields were corrected for small mismatches between the Monte-Carlo sim-432 ulation of the spectrometers and the actual acceptance. Three-dimensional grids in relative 433 momentum (dp/p), in-plane scattering angle (yptar), and vertical angle (xptar) of the de-434 tected particles were constructed by minimizing the  $\chi^2$  to achieve agreement among data 435 taken at different central momenta and scattering angles, using the entire data set of this 436 experiment. The multiplicative correction factors, shown in Fig. 12, are applied to the 437 event-by-event weights for events generated in SIMC. For the HMS spectrometer, the most 438 prominent feature is a "dip" near dp/p = -2% for the central scattering angles, with only 439 minor dependence on out of plane angle. This feature was been noted before in previous one-dimensional studies that only looked at the dependence on dp/p. This new 3D study shows that the "dip" becomes more of a "bump" at larger absolute values of yptar, and 442 also shows some non-trivial xptar dependence. The SHMS spectrometer was new for this 443 experiment, so our acceptance study is the first one. We found little dependence on vertical 444 angle in the region -0.03 < xptar < 0.03 rad, where the bulk of the data reside. We found 445 a considerable dp/p dependence which itself is significantly dependent on scattering angle. 446

## F. Event Selection Cuts and Efficiency Corrections

The SIMC weights were also corrected event-by-event for the detector efficiencies, which
can vary with position in the spectrometer hut, especially for the heavy gas Cherenkov
detector in the SHMS. The same event selection cuts were used on the SIMC track positions
at the HMS and SHMS detectors, spectrometer exit apertures, and reconstructed momenta
and angles as for the actual experimental data. An overall factor of 0.99 was applied to

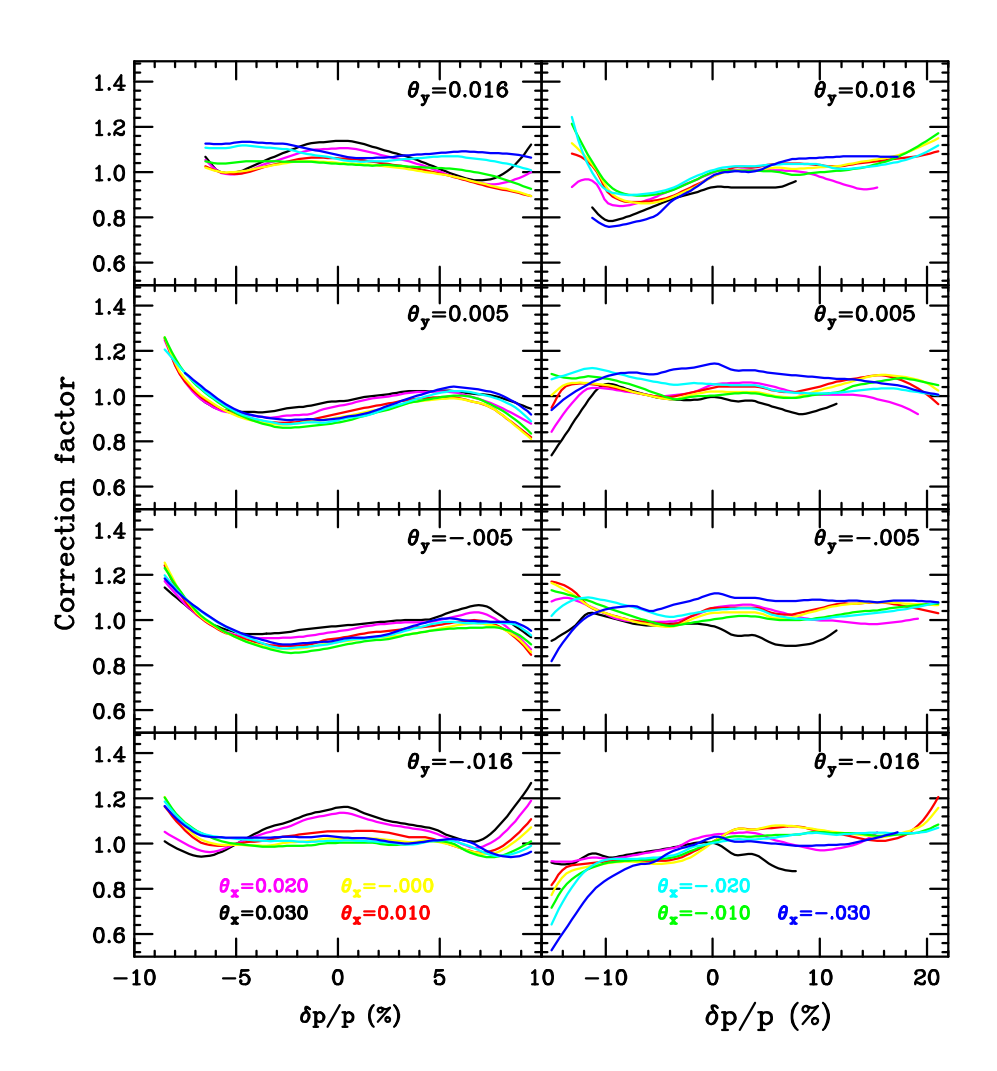


FIG. 12. Acceptance correction factors as a function of dp/p for four bins in in-plane relative scattering angle  $\theta_y$  for HMS (left-hand column) and SHMS (right-hand column). The different colors correspond to bins in out-of-plane angle  $\theta_x$ .

account for pion absorption in the target.

The quality of the models and corrections used in the simulation is demonstrated in Fig. 13, showing the excellent agreement between the experimental yields and simulated yields for setting I with the SHMS spectrometer centered on z = 0.9 to capture the contributions for exclusive pion production (centered on electron-pion missing mass  $M_x = 0.94$ GeV),  $\pi\Delta$  electroproduction (centered on  $M_x = 1.232$  GeV), and high-z SIDIS from both the target liquid and endcap.

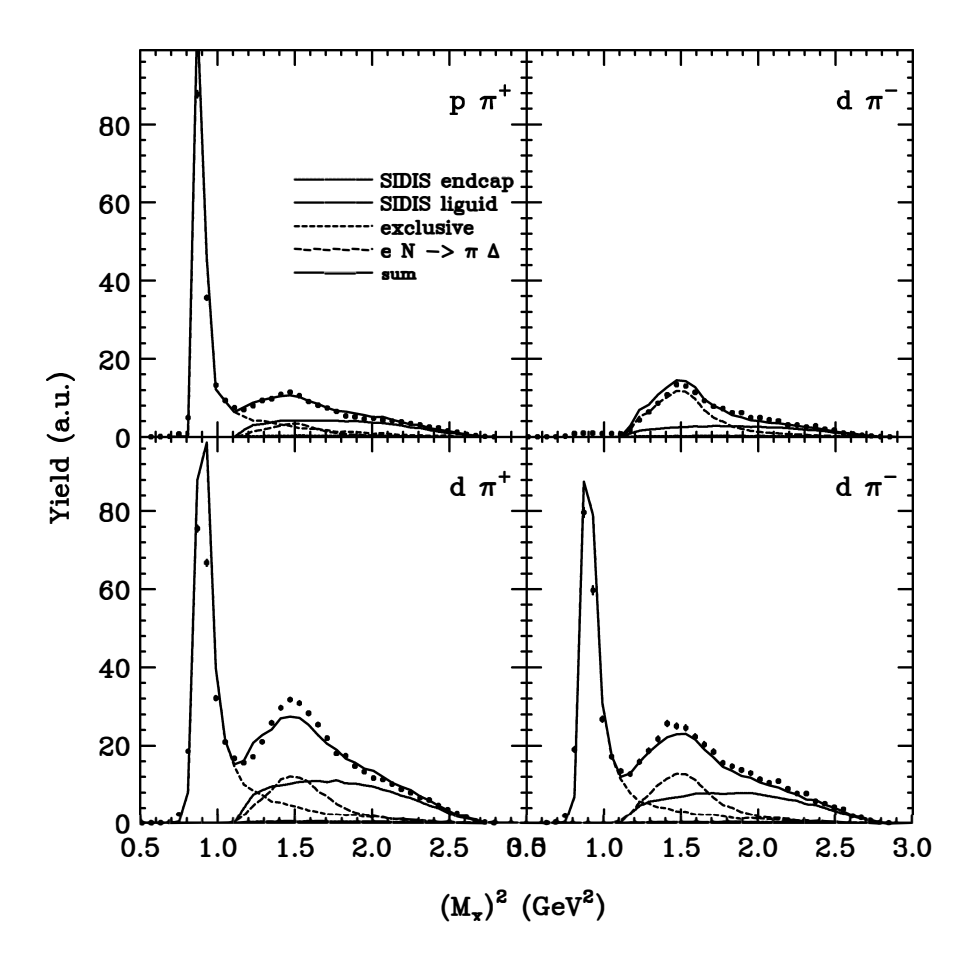


FIG. 13. Experimental yields as a function of electron-pion missing mass squared for setting I from auxiliary runs taken with the SHMS centered on z=0.9, compared to the predicted Monte-Carlo yields for SIDIS, exclusive pion production, and  $\pi\Delta$  production. Results are shown for both  $\pi^+$  (left panels) and  $\pi^-$  production (right panels) and proton (top row) and dueteron targets (bottom row).

## 461 IV. RESULTS

462

# A. Data Analysis

For each set of data with identical settings and target, the number of electron-pion coincidences, corrected for accidental and target endcap contributions, were divided by the accumulated beam charge to form an experimental yield  $Y_{exp}$ .

The corrected yields were binned in a 3-dimensional grid with twenty bins in z from 0 to 1, 16 bins in  $P_t$  from 0 to 1, and 15 bins in  $\phi^*$  from 0 to  $2\pi$ . The predicted yields  $Y_{MC}$ 

from the MC simulation of each data set were accumulated into the same kinematic grid 468 as the experimental data. The simulated yields included contributions from SIDIS itself as 469 well as the radiative tails from the exclusive pion and  $\pi\Delta$  reactions. The predicted yields 470 were corrected for all detector and PID efficiencies as well as the luminosity dependence. 471 The same detector position, magnet aperture, and reconstructed track variables were used 472 as for the experiment data. 473

Experimental multiplicities, defined as the ratio of the SIDIS cross section  $(d\sigma_{ee'\pi X})$  to 474 the inclusive DIS cross section  $(d\sigma_{ee'X})$ , were determined for each kinematic bin by: 475

$$M_i(z, P_t, \phi^*) = M_0(x, Q^2, z, P_t, \phi^*) \frac{Y_{exp}}{Y_{MC}}$$
 (9)

for each target nucleus (p/d), HMS polarity, and  $(x,Q^2)$  HMS setting, where  $M_0$  is the 476 multiplicity model used in the MC simulation, evaluated at the center of each bin, and the 477 index i covers the SHMS settings that provide overlap in  $(z, P_t, \phi^*)$ . In most cases, there 478 were two overlapping settings, but occasionally there were three or four overlaps. The final results were taken as the weighted average of  $M_i$ .

The results discussed in this paper included the addition cut  $M_x > 1.6$  GeV, to remove the region where contributions from nucleon resonances, semi-exclusive processes, and higher-482 twist effects appear to be large, as shown in Fig. 2. This cut was removed for a version of 483 the analysis used to iterate the SIDIS model used in the MC simulation.

481

484

Numerical results for the multiplicities are tabulated in a full three-dimensional grid in 485  $(z, P_t, \phi^*)$  for each target, pion polarity, and HMS setting in  $(x, Q^2)$  on the Hall C experimen-486 tal results web page [37]. In this table, each HMS spectrometer setting was divided in two, 487 with relative scattering angle either positive or negative. A total of 20,000 bins are listed, 488 based on the criteria that the Monte Carlo simulation prediction was for more than 4 counts, 489 to ensure approximately Gaussian statistical errors on the experimental data. The table also 490 includes results from thirteen additional HMS settings taken in Fall 2018 and Spring 2019 to 491 study charge-symmetry violation in pion fragmentation functions, as reported in Ref. [30]. 492 These settings covered a small range  $\langle P_t \rangle \sim 0.1$  GeV, and therefore are not included in 493 the results of the present publication. The tables also include multiplicity results with no 494 radiative corrections applied, which may prove useful in future global fits with consistent 495 radiative correction models and formalism.

# B. Pion multiplicities as a function of $(z, P_t, \phi^*)$

497

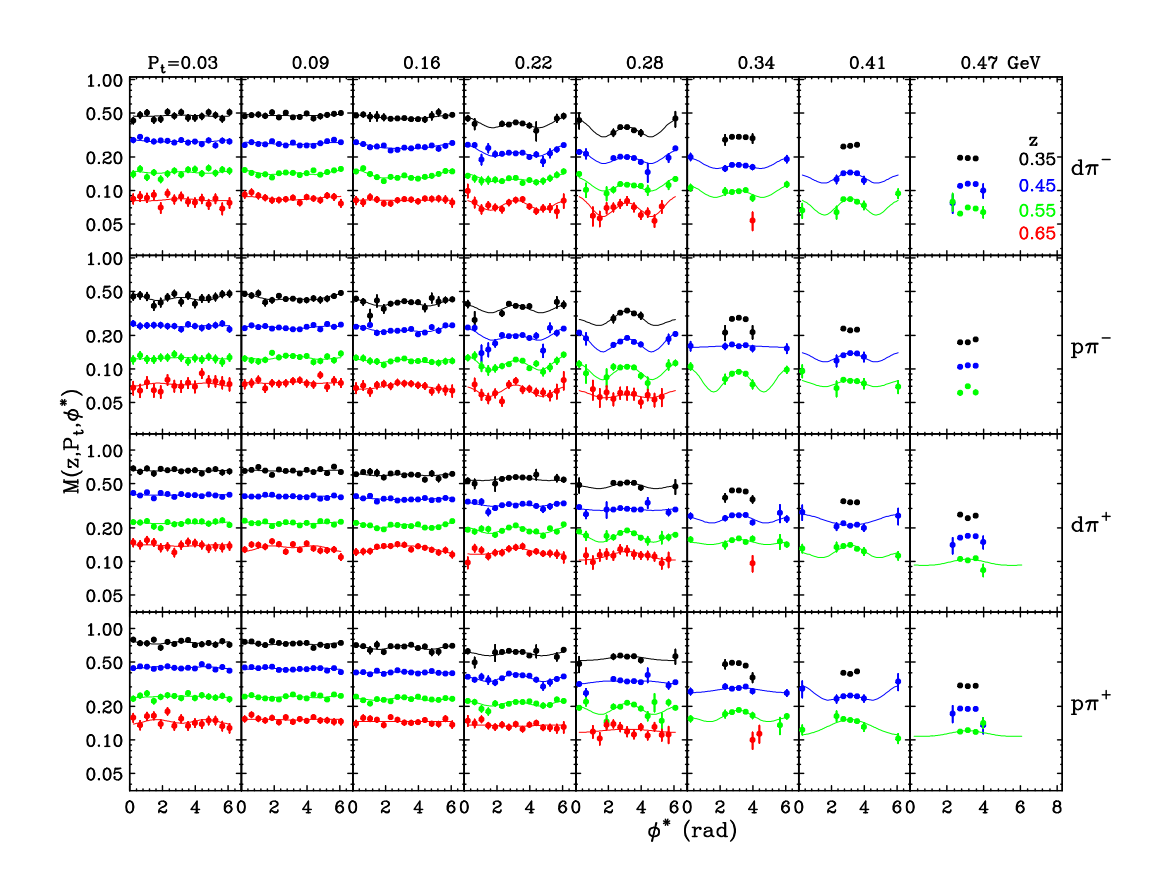


FIG. 14. Pion multiplicity as a function of  $\phi^*$  for x = 0.31,  $Q^2 = 3 \text{ GeV}^2$  (kinematic setting I) for five bins in  $P_t$  (left to right) and four target/final state configurations (top to bottom), for five values of z as indicated on the right edge of the rightmost panels. The solid curves are fits to each data set at fixed z,  $P_t$ , target, and pion charge with the functional form  $M_0[1 + A\cos(\phi^*) + B\cos(2\phi^*)]$ .

The  $\phi^*$  dependence of the semi-inclusive pion electroproduction multiplicity  $M(x,Q^2,z,P_t,\phi^*)$  is shown in discrete bins of z and  $P_t$  for kinematic setting I ( $x=0.31, Q^2=3.1 \text{ GeV}^2$ , W=2.8 GeV) in Fig. 14. For clarity, adjacent bins in z had been combined together, and only the first five bins in  $P_t$  are shown: as higher values of  $P_t$  the  $\phi^*$  coverage becomes increasingly centered near 180 degrees due to the use of in-plane spectrometers in this experiment. Similarly, the results for settings II and III are shown in Fig. 15 and Fig. 16 respectively.

The main features of the data are:

505

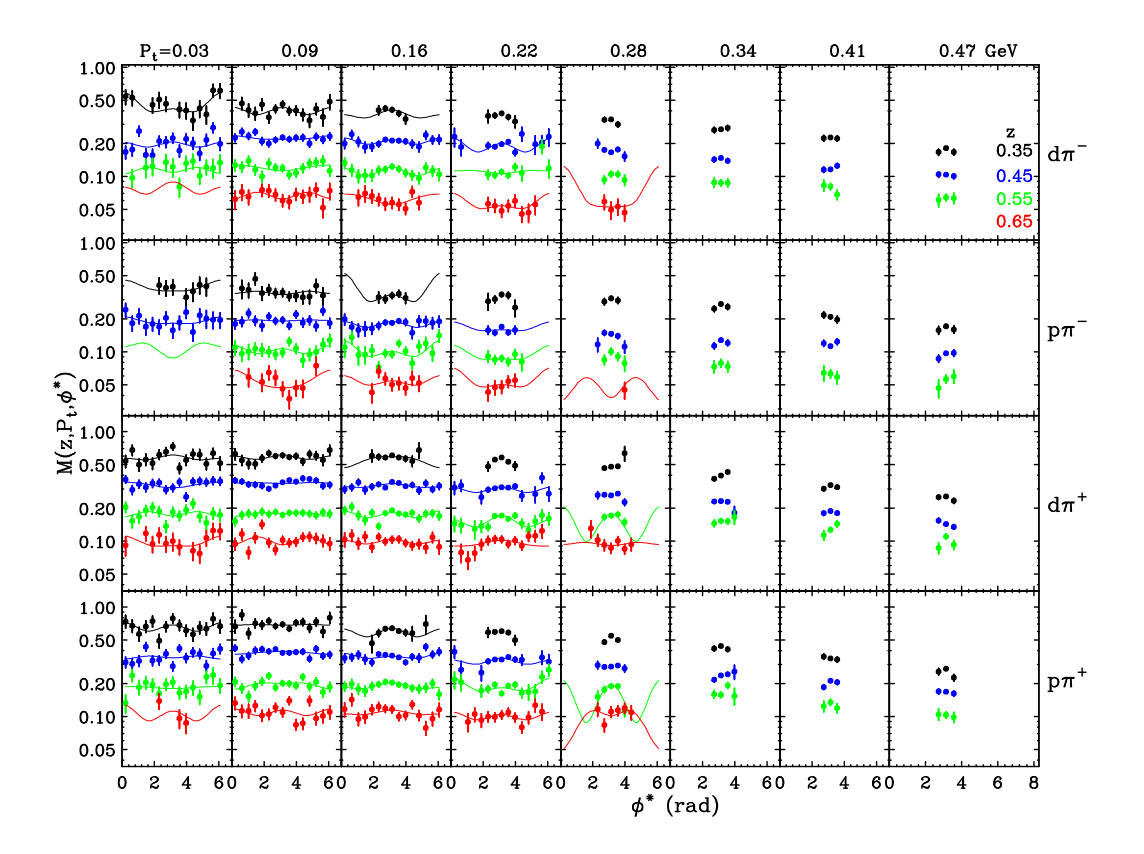


FIG. 15. Same as Fig. 14 except for x = 0.30,  $Q^2 = 4.1 \text{ GeV}^2$  (kinematic setting II).

- 506 a) the multiplicity decreases with increasing z;
- b) the multiplicity decreases with increasing  $P_t$ ; and
- 508 c) the distributions tend to be mostly independent of  $\phi^*$  at fixed values of z and  $P_t$ .

To quantify this behavior, each data set at fixed z,  $P_t$ , target, and pion charge was fit with the functional form

$$M_0[1 + A\cos(\phi^*) + B\cos(2\phi^*)].$$
 (10)

In terms of the standard structure functions [3],

$$M_0 = (F_{UU,T} + \epsilon F_{UU,L})/(F_T + \epsilon F_L)$$

$$A = \sqrt{2\epsilon(1 + P_t)} F_{UU}^{\cos(\phi^*)}/(F_{UU,T} + \epsilon F_{UU,L})$$

$$B = P_t F_{UU}^{\cos(2\phi^*)}/(F_{UU,T} + \epsilon F_{UU,L})$$

The fit results are discussed in the next subsections.

511

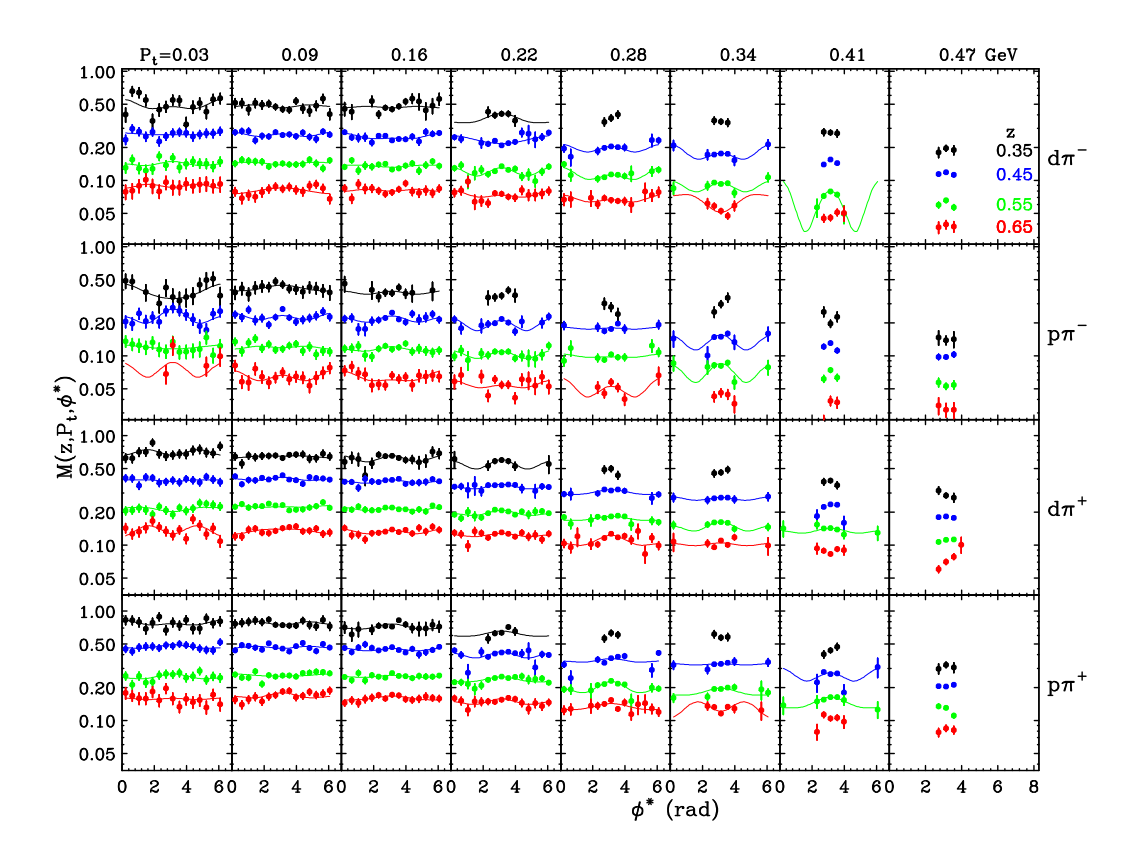


FIG. 16. Same as Fig. 14 except for  $x=0.45,\,Q^2=4.5~{\rm GeV^2}$  (kinematic setting III).

# C. Pion multiplicities averaged over $\phi^*$

The results for the  $\phi^*$  averaged parameter,  $M_0$ , from the fits described above are displayed in Fig. 17 as a function of  $P_t$  for the three kinematic settings, the target and pion charge combinations, in four bins in z. The measured multiplicities are compared to the calculation of MAPS [38–40] scaled by a  $P_t$ -independent normalization factors k that give the best agreement with these data. The MAPS calculations, which uses a combination of Gaussian and weighted Gaussian distributions in  $P_t$  based on a fit to data from HERMES and COMPASS, are generally in good agreement with the measured  $P_t$  dependence.

It is of particular interest to compare the  $P_t$  dependence of  $M_0$  for the four target and pion charge combinations. A large difference at high z between positive and negative pions could originate from different  $k_t$  width of the up and down PDFs, while large differences at lower z could be ascribed to different  $P_t$  widths in favored fragmentation compared to unfavored fragmentation functions. The results shown in Fig. 17 don't show any obvious

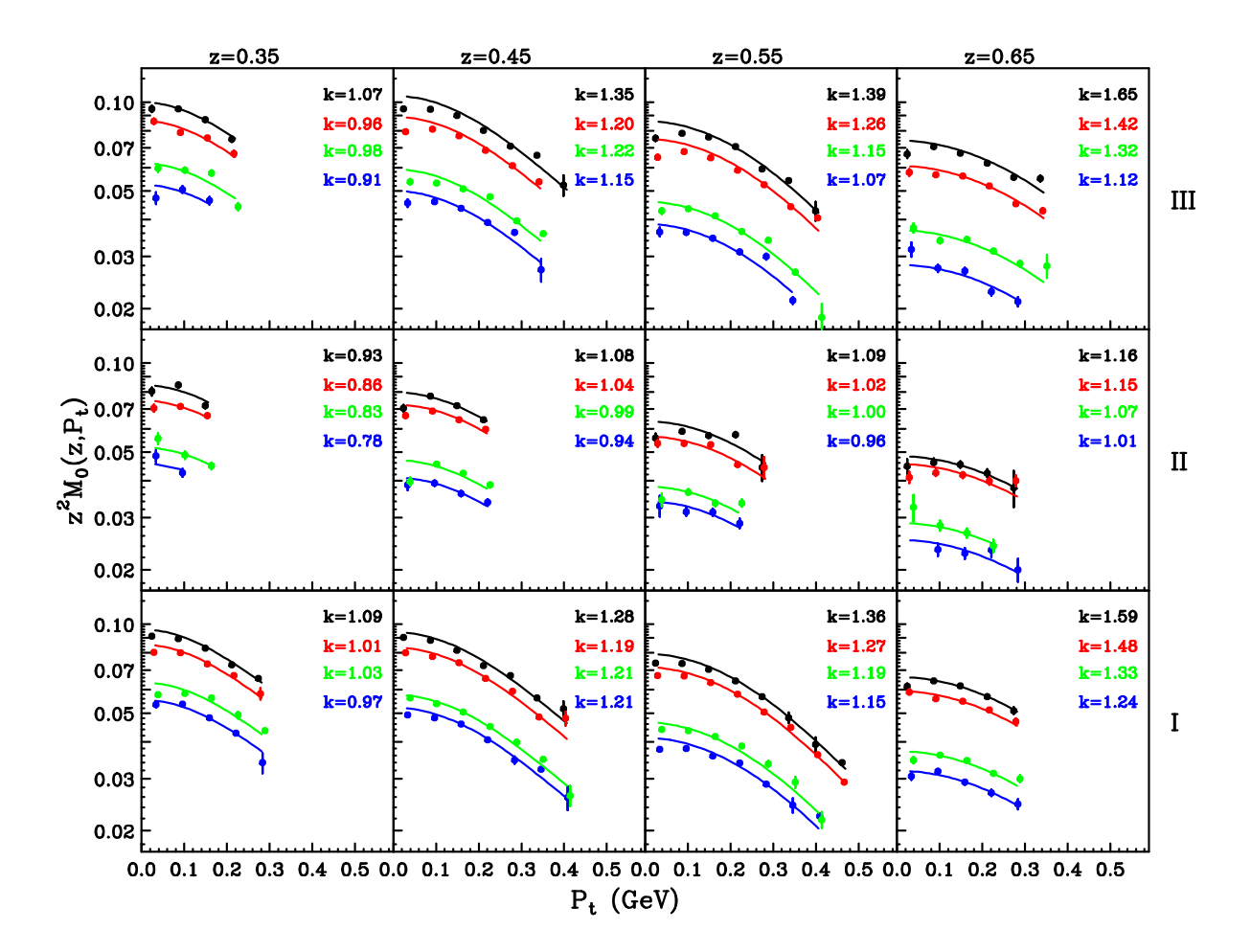


FIG. 17. The  $\phi^*$  averaged fit parameter  $M_0$  weighted by  $z^2$ , as a function of  $P_t$ , for the three kinematic settings of this experiment (top to bottom) in four bins in z (left to right). Within each panel, the results from top to bottom are for  $\pi^+$  from a proton target (black),  $\pi^+$  from a deuteron target (red),  $\pi^-$  from a deuteron target (green) and  $\pi^-$  from a proton target (blue). The curves are the predictions of the MAPS collaboration based on a fit to previous world data [38–40], normalized with a parameter k to give the best overall agreement with these results.

flavor dependence in most cases.

The  $P_t$ -independent normalization factors k are plotted in Fig. 18 as a function of z, for the target and pion charge combinations and the three kinematic settings. They are, on average, closest to unity for setting II (W = 3.3 GeV), and tend to be larger than unity for setting I (W = 2.8 GeV), and even larger for setting III (W = 2.6 GeV). There is also a clear trend for k to increase with increasing z, especially for positive pions from the proton target, and to a lesser extent for the positive pions from the deuteron target. These trends

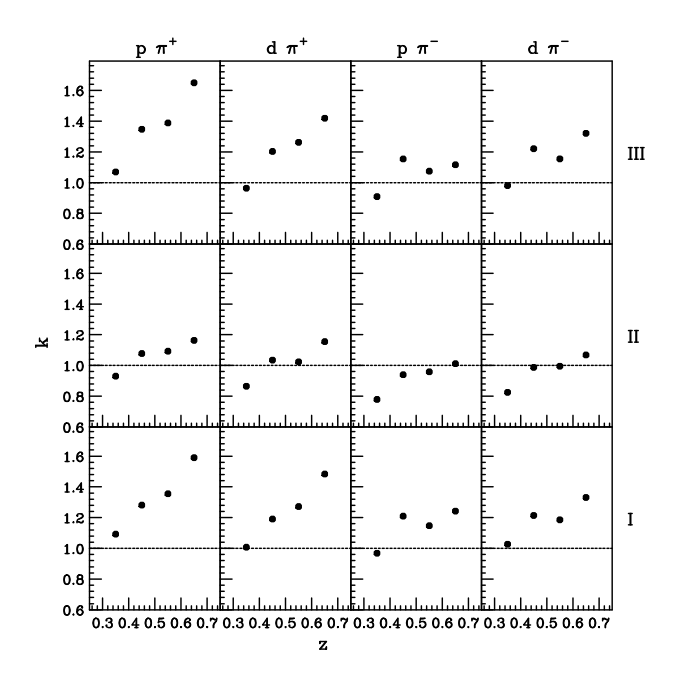


FIG. 18. Normalization factors k that best describe fit the MAPS calculations [38–40] for the three kinematic settings of this experiment (top to bottom) and the four flavor cases (left to right).

are likely related to the fact that the present data are at lower W and higher x than the HERMES and COMPASS data that went into the MAPS global fit.

To further quantify the observed flavor independence of the multiplicities, the ratio of multiplicities for  $(p, \pi^+)$ ,  $(p, \pi^-)$ , and  $(d, \pi^-)$  to the multiplicities for  $(d, \pi^+)$  are plotted in Fig. 19 as a function of  $P_t$  for the three kinematic settings and four z bins. The ratios are generally very consistent with no dependence on  $P_t$ . The ratios are compared to those from the MAPS calculations [38–40], which also show only very slight  $P_t$  dependence. As expected from the discussion on normalization factors (k parameter) above, the ratios for  $(p, \pi^+)$  are larger for the data than for the calculations, especially for the lower W kinematic settings.

Due to the experimental setup limitations, it was not possible to obtain full azimuthal coverage at large  $P_t$ . Nonetheless, a considerable amount of time was spent accumulating data near  $\phi^* = 180^\circ$ , where we basically measure  $M_0(1 - A + B)$ . Given this caveat, it is of interest to plot the flavor ratios at  $\langle \phi^* \rangle \sim 180^\circ$ , over the full  $P_t$  experimental range, as shown in Fig. 20. The multiplicity ratios relative to  $(p, \pi^+)$ , as described above, at  $\langle \phi^* \rangle \sim 180^\circ$  appear to be relatively constant all the way up to  $P_t = 0.7$  GeV, in most cases, thus placing additional constraints on the the flavor dependence of quark  $\langle k_t \rangle$  values and fragmentation

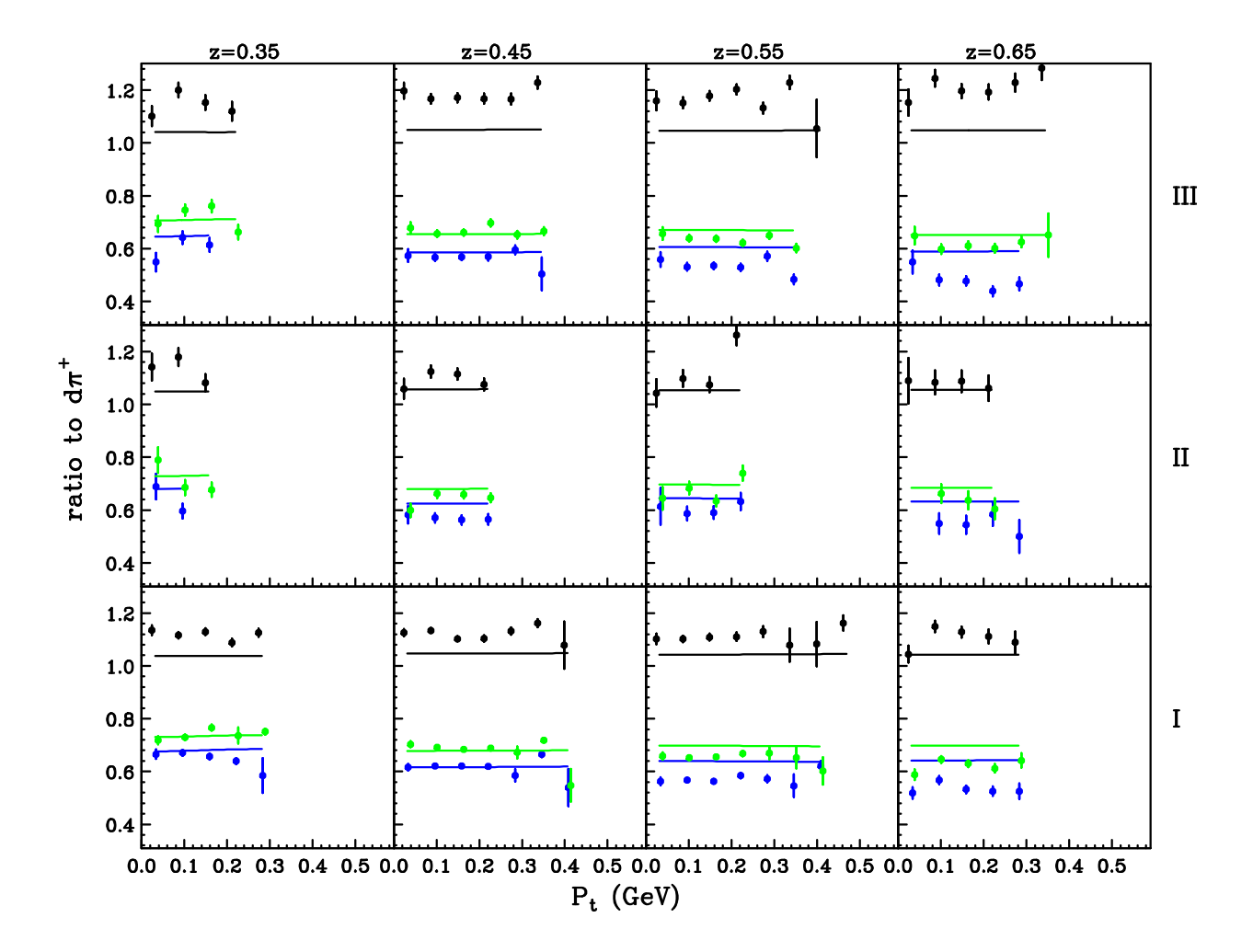


FIG. 19. Ratios of  $M_0$  for  $\pi^+$  from a proton target (black),  $\pi^-$  from a deuteron target (green) and  $\pi^-$  from a proton target (blue) divided by  $M_0$  for  $\pi^+$  from a deuteron target. The format is the same as for Fig. 17. The curves are the ratios of the MAPS calculations [38–40].

function  $\langle P_t \rangle$  values. The curves on this plot are the ratios of the MAPS calculations.

(MAPS did not include non-zero values of A and B in their fits).

## D. Azimuthal dependence of Multiplicities

551

The  $\phi^*$  dependence of the measured multiplicities is quantified by the two coefficients, A and B, associated with the  $\cos(\phi^*)$  and  $\cos(2\phi^*)$  modulation of the multiplicities. The  $\cos(\phi^*)$  coefficient, A, obtained from the fit of the multiplicity results in each  $(z, P_t)$  bin to functional form Eq. 10, is shown in Fig. 21 as a function of  $P_t$ . These results show an overall trend that A for  $\pi^-$  production on both protons and deuterons is significantly > 0

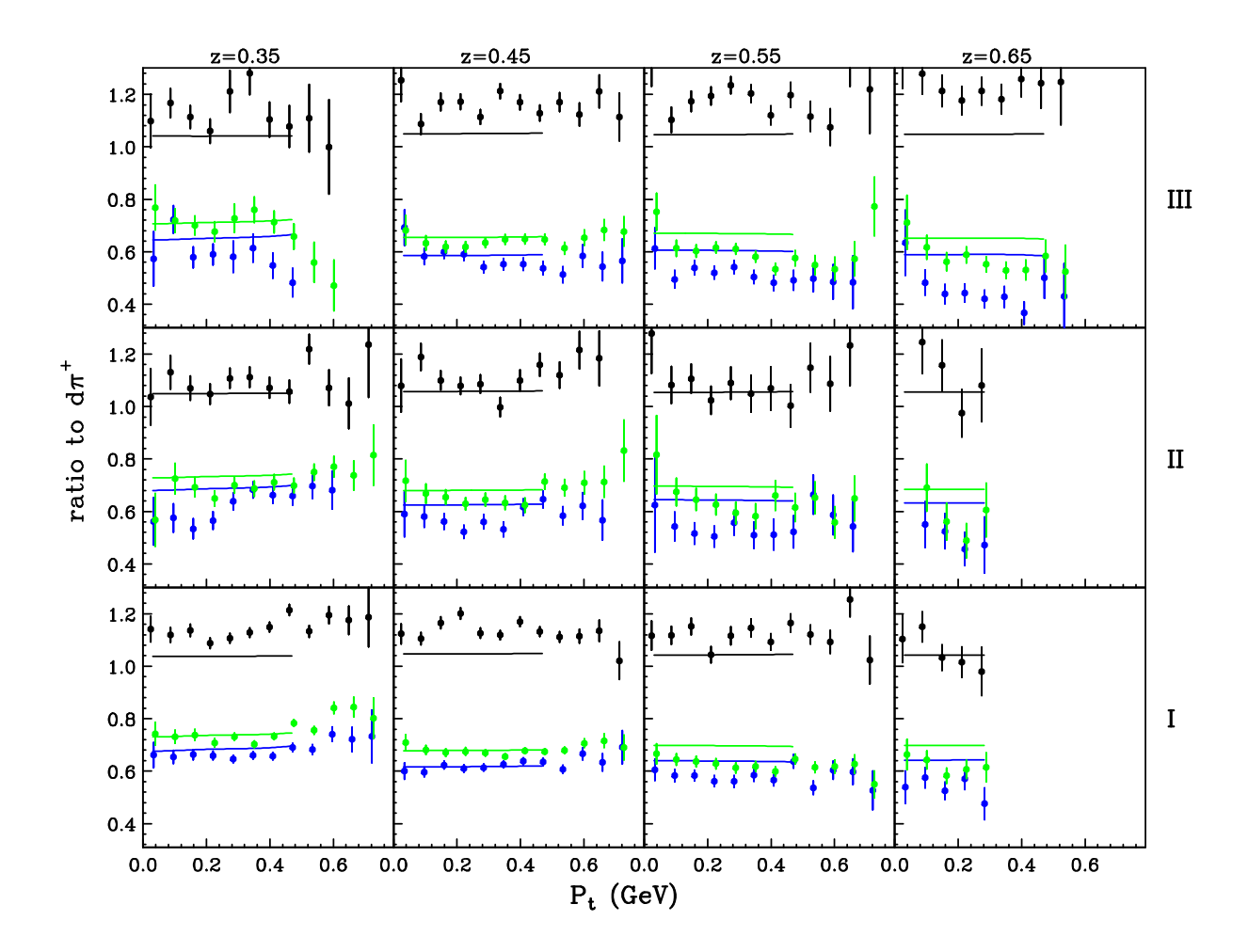


FIG. 20. Same as Fig. 19 but now for the experimental multiplicities averaged over  $150 < \phi^* < 210$  degrees.

at high z for all three kinematic settings. On the other hand the A coefficient is consistent with zero within experimental uncertainties or has a small negative values for  $\pi^+$  production on both protons and deuterons. The  $\pi^+$  results are consistent with the previous HERMES measurements but have the opposite sign for the  $\pi^-$ .

Similarly the  $\cos(2\phi^*)$  coefficient, B, obtained from the fit of the multiplicity results in each  $(z, P_t)$  bin to Eq. 10 is shown in Fig. 22 as a function of  $P_t$ . Other than a couple of z bins these results show small values of B that are either consistent with zero or have small positive values. These results are consistent with the previous HERMES measurements except at  $\langle z \rangle = 0.55$ .

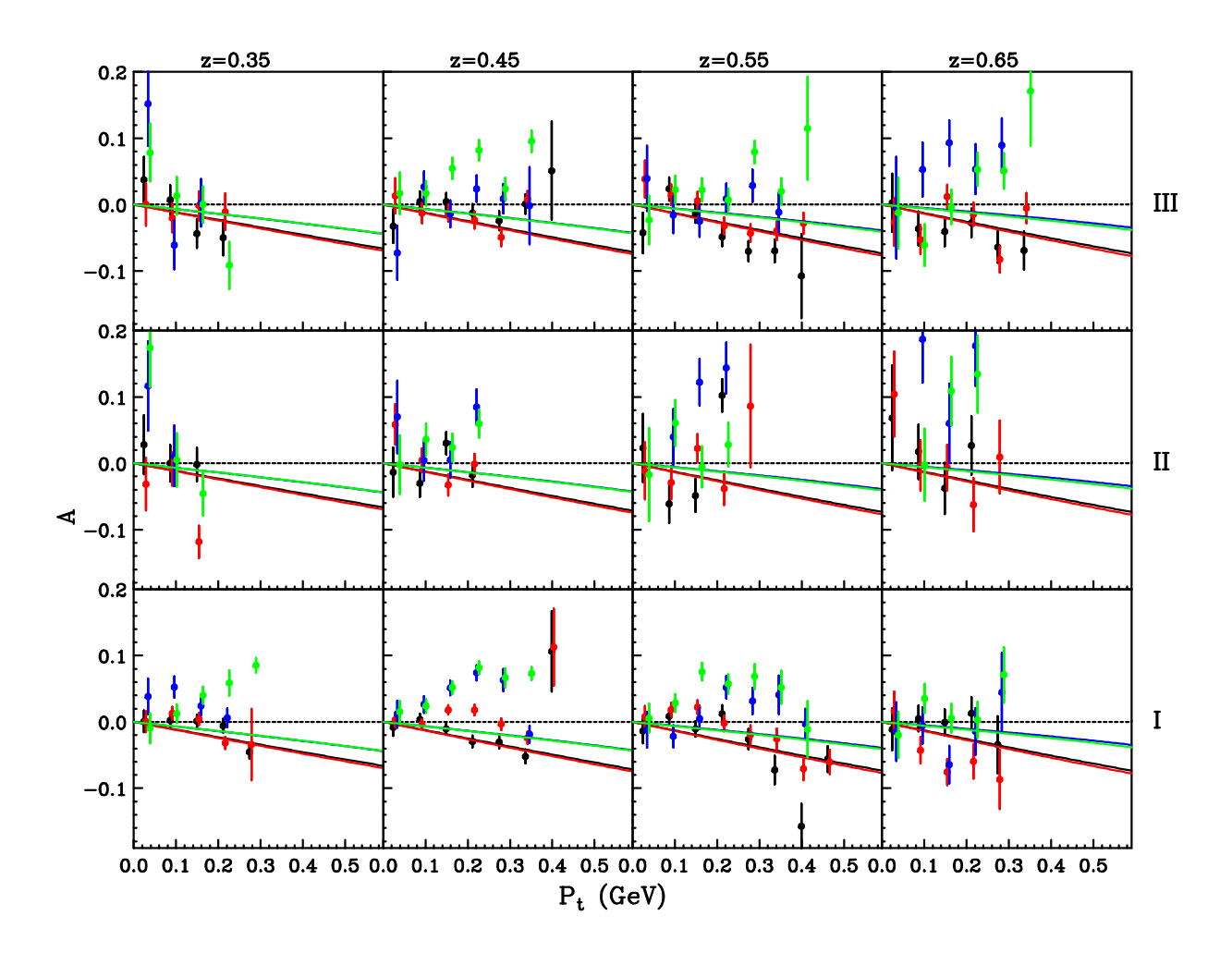


FIG. 21. Results for the coefficients A that scale the  $\cos(\phi^*)$  distributions, in the same format as Fig. 17. The dashed curves are from a fit to HERMES data [15].

# E. Systematic Uncertainties and caveats

# F. Experimental systematic studies

The entire analysis was performed with several alternate sets of cuts and PID criteria. One study used a smaller range in track momenta and angles. Another ignored the heavy gas detector in the HMS, which generated significant kaon contamination of the pion sample above momenta of 3 GeV. A third study used a lower aerogel threshold, with correspondingly larger kaon contamination subtraction. The luminosity and HMS acceptance were verified to be accurate within 3% by comparison of elastic electron-proton measurements to a fit to global data [41]. The optical properties of the spectrometers were verified using the kinematic constraints of both *ep* elastic scattering and exclusive pion production.

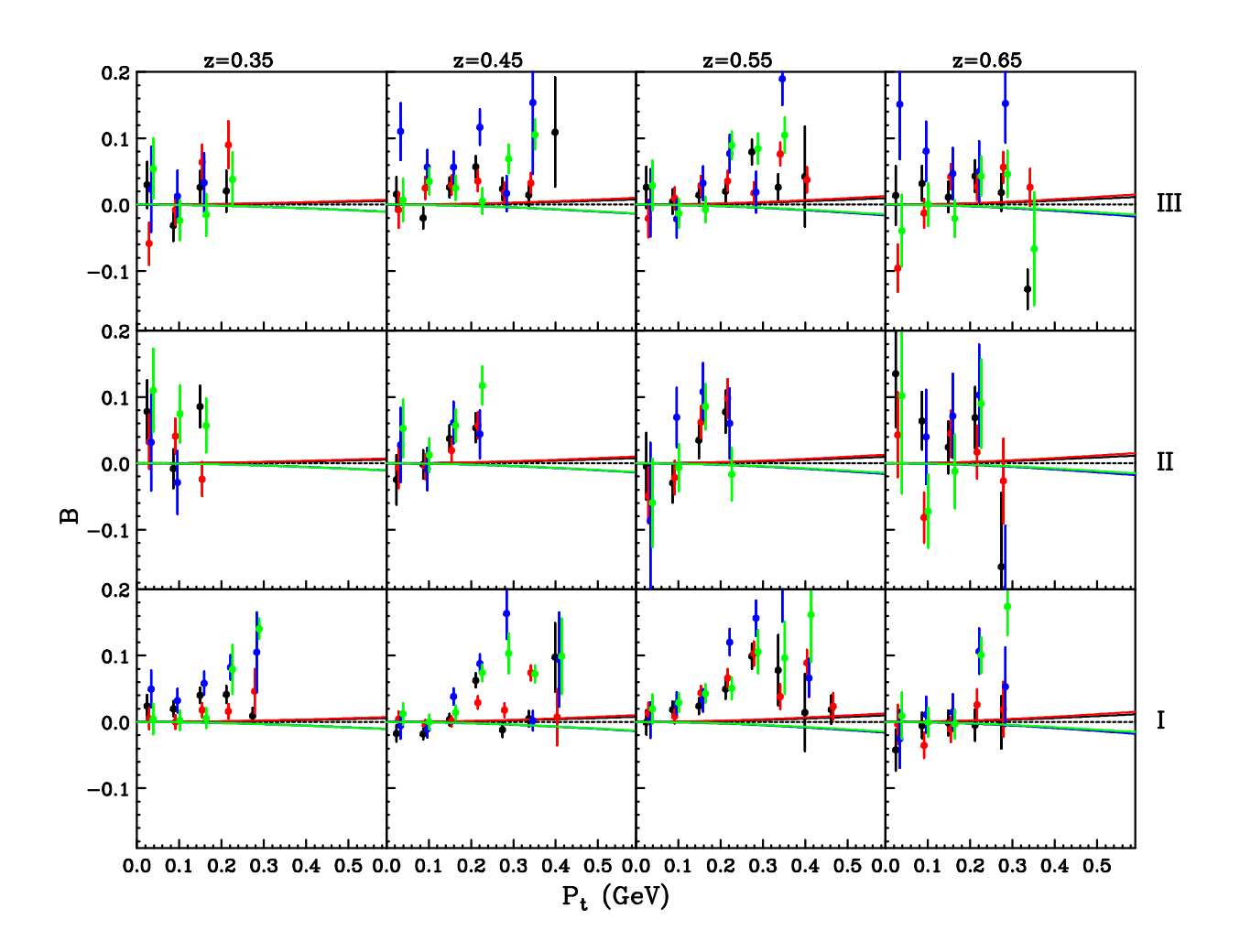


FIG. 22. Results for the coefficients B that quantifies the  $\cos(2\phi^*)$  modulation.

## G. Experimental systematic errors

The main sources of systematic uncertainties are listed in Table VI, based on the studies mentioned above as well as known instrumental uncertainties. They have been divided into two categories; normalization/scale uncertainties that impact all measurements on a given target equally, and point-to-point uncertainties that vary with pion kinematics and charge. The overall experimental systematic error is estimated to be about 2.5% for setting III. Due to many problems in Spring 2018, we estimate an additional overall normalization error of 2% for settings I and II.

TABLE VI. Principal experimental Systematic uncertainties, divided in overall normalization (scale) uncertainties and those that vary with pion kinematics.

Source	Scale	Point-to-Point
	Uncertainty (%)	Uncertainty (%)
Charge	-	0.5
Target density	1	-
Target boiling correction	-	0.3
Target end cap subtraction	0.3	-
Particle identification	1	-
PID Purity	-	0.2
Spectrometer Acceptance	1	0.5
Kinematics	-	0.3
Rate dependence	-	1
Total	2	1.3

# H. Radiative corrections

584

The application of radiative corrections is ideally an iterative process in which all available 585 global data are iteratively analyzed until convergence is achieved. For the present analysis, 586 we rely on our fits to the world data (including our own) on three physics processes: exclusive 587 pion production,  $\Delta$  resonance production, and  $\rho$  meson production. Our fit to exclusive pion 588 production is driven largely by preliminary, unpublished results from Hall C experiments 589 conducted between 2018 and 2022. The combined statistical and systematic error on the 590 fit is of the order 5% for  $\pi^+$  and 10% for  $\pi^-$  (applicable only for the deuteron target). 591 Since the radiative tail from exclusive pion production varies from 1% to 10%, we estimate 592 a model uncertainty of 0.1-0.5% (0.2-1%) for the exclusive pion radiative tails to  $\pi^+$ 593  $(\pi^{-})$  production. Due to lack of available data, our simple fit to  $\pi\Delta$  production is much less 594 certain, resulting in a range of 0.5-3% uncertainty, depending on pion kinematics. The 595 ratio of radiated to unradiated SIDIS cross sections is relatively insensitive to the absolute 596 normalization of the model and is primarily driven by the kinematic dependence on z and 597  $P_t$ . Based on our iterations of the model, we estimate about 1% uncertainty in the radiative corrections due to the SIDIS model, roughly independent of pion kinematics.

Other sources of radiative correction uncertainty could arise from the use of the anglepeaking approximation (photons emitted only along the incident or scattered electron direction), the uncertainty in the soft-photon term, use of the equivalent radiator approximation, the neglect of pion radiation, and the lack of two-photon corrections.

We have listed our results [37] both with and without radiative corrections, allowing for future improvements.

## I. Interpretation Systematics

Due to a lack of experimental data in our kinematic region, we have not corrected our results for the contributions from diffractive exclusive vector meson production. This contribution was studied by the COMPASS collaboration [42], which found substantial corrections to  $\langle cos(\phi^*) \rangle$  and  $\langle cos(2\phi^*) \rangle$  for x < 0.05, but very small corrections for x > 0.1, where all of the present data lie.

The data in this paper were taken at a single beam energy, and thus cannot be used to separate the transverse and longitudinal structure functions.

# 614 V. SUMMARY

606

In summary, we have measured the  $\pi^{\pm}$  multiplicaties from SIDIS on H and D targets 615 over a range of z,  $P_t$ , and  $\phi^*$ . The results indicate that the the  $\phi^*$ -averaged multiplicities 616 cannot be described by a single Gaussian  $P_t$  dependence. They are best described by a 617 combination of Gaussian and weighted Gaussian distributions in  $P_t$ . The shape of the  $P_t$ 618 dependence of the multiplicities are also found to be independent of the electron kinematics, 619 the pion charge, as well as target type (p/d). The  $\cos(\phi^*)$  modulation for the  $\pi^-$  is found 620 to be greater than zero, deviating significantly from the expectations of the "Cahn Effect", 621 however, they are consistent with expectations for the  $\pi^+$ . The  $\cos(2\phi^*)$  modulations are 622 found to be consistent with zero for all charged pions. The fits that are consistent with the 623 data for  $P_t < 0.25$  GeV generally do not agree with the data when extrapolated to higher  $P_t$  and  $\phi^*$  around 180°. When these data are included in future global fits of PDF and FF 625 including higher-order corrections, they will provide further detailed insight into the SIDIS 626 process and associated higher order corrections. 627

### 628 VI. ACKNOWLEDGMENTS

- We are grateful to M. Cerutti for providing calculations of the 2022 MAPS model at each of the kinematic settings of this experiment
- This work was funded in part by the U.S. Department of Energy, including contract
- AC05-06OR23177 under which Jefferson Science Associates, LLC operates Thomas Jefferson
- National Accelerator Facility, and by the U.S. Department of Energy, Office of Science,
- contract numbers DE-AC02-06CH11357, DE-FG02-07ER41528, DE-FG02-96ER41003, and
- by the U.S. National Science Foundation grants PHY 2309976, 2012430 and 1714133 and the
- Natural Sciences and Engineering Research Council of Canada grant SAPIN-2021-00026. We
- wish to thank the staff of Jefferson Lab for their vital support throughout the experiment.
- We are also grateful to all granting agencies providing funding support to authors throughout
- this project.
- [1] M. Anselmino, M. Boglione, U. D'Alesio, A. Kotzinian, F. Murgia, and A. Prokudin, Phys.
   Rev. D 71, 074006 (2005).
- [2] M. Anselmino, A. Efremov, A. Kotzinian, and B. Parsamyan, Phys. Rev. D 74, 074015
   (2006).
- [3] A. Bacchetta, M. Diehl, K. Goeke, A. Metz, P. Mulders, and M. Schlegel, J. of High Eng. Phys. **02**, 093 (2007).
- <sup>646</sup> [4] P. Mulders and R. Tangerman, Nucl. Phys. B **461**, 197 (1996).
- [5] D. Boer, P. J. Mulders, and O. V. Teryaev, Phys. Rev. D 57, 3057 (1998), arXiv:hep ph/9710223.
- 649 [6] X. Ji, J.-P. Ma, and F. Yuan, Phys. Lett. B **597**, 299 (2004).
- 650 [7] T. Navasardyan *et al.*, Phys. Rev. Lett. **98**, 022001 (2007).
- 651 [8] H. Mkrtchyan, P. E. Bosted, et al., Phys. Lett. B 665, 20 (2008).
- 652 [9] M. Osikenki *et al.*, Phys. Rev. D **80**, 032004 (2009).
- 653 [10] R. Asaturyan et al., Phys. Rev. C 85, 015202 (2012).
- 654 [11] M. Anselmino et al., Eur. Phys. J. A 47, 35 (2011).
- 655 [12] V. Barone, F. Bradamante, and M. A., Prog. Part. Nucl. Phys **65**, 267 (2010).

- 656 [13] A. Bacchetta and M. Radici, Phys. Rev. Lett. 107, 212001 (2011).
- [14] M. Anselmino, M. Boglione, J. O. Gonzalez-Hernandez, S. Melis, and A. Prokudin, J. of High
   Eng. Phys. 04, 005 (2014).
- [15] V. Barone, M. Boglione, J. O. Gonzalez Hernandez, and S. Melis, Phys. Rev. D 91, 074019
   (2015).
- [16] A. Bacchetta, F. Delcarro, C. Pisano, M. Radici, and A. Signori, J. of High Eng. Phy. 06, 81
   (2017).
- 663 [17] R. N. Cahn, Phys. Lett. B 78, 269 (1978).
- 664 [18] D. Boer and P. J. Mulders, Phys. Rev. D **57**, 5780 (1998).
- 665 [19] J. Collins, Nuclear Physics B **396**, 161 (1993).
- [20] C. J. Bebek, C. N. Brown, M. Herzlinger, S. D. Holmes, C. A. Lichtenstein, F. M. Pipkin,
   S. Raither, and L. K. Sisterson, Phys. Rev. Lett. 34, 759 (1975).
- 668 [21] J. Ashman et al. (EMC), Z. Phys. C 52 (1991) 361-388 **52**, 361 (1991).
- 669 [22] A. Airapetian et al. (HERMES), Phys. Rev. D 87, 074029 (2013), arXiv:1212.5407 [hep-ex].
- [23] C. Adolph *et al.* (COMPASS), Eur.Phys.J.C **73**, **(2013) 8**, 2531, erratum Eur.Phys.J.C **75** (2015) 2, 94, arix.1305.7317 [hep-ex].
- 672 [24] H. Mkrtchyan, P. Bosted, R. Ent, E. Kinney, et al., Jefferson Lab experiment E12-09-017.
- 573 [25] SURA-CEBAF, ""cebaf conceptual design report, basic experimental equipment", newport news, virginia, 1990," https://digital.library.unt.edu/ark:/67531/metadc674902/.
- [26] H. Mkrtchyan et al., Nucl. Inst. and Meth. A **719**, 85 (2013).
- 676 [27] S. Ali et al., arXiv:2503.08706 [physics.ins-det], https://arxiv.org/pdf/2503.08706.
- 677 [28] CLAS Collaboration, Jefferson Lab, https://www.jlab.org/physics/hall-b/clas.
- 678 [29] CLAS12 Collaboration, Jefferson Lab, https://www.jlab.org/physics/hall-b/clas12.
- 679 [30] H. Bhatt *et al.*, Physics Letters B **865**, 139485 (2025).
- [31] H. Bhatt, PhD Dissertation, Mississippi State University, 2024. https://misportal.jlab.org/sti/publications/23431.
- [32] S. Jia, PhD Dissertation, Temple University, 2022. https://misportal.jlab.org/sti/ publications/21868.
- 684 [33] CEBAF Data Acquisition System (DAQ), https://coda.jlab.org.
- 685 [34] Hall C MC, https://hallcweb.jlab.org/wiki/index.php/SIMC\_Monte\_Carlo,.
- 686 [35] L. W. MO and Y. S. TSAI, Rev. Mod. Phys. 41, 205 (1969).

- [36] S. Kuhlmann, Nuclear Physics B Proceedings Supplements **79**, 108 (1999), proceedings of the 7th International Workshop on Deep Inelastic Scattering and QCD.
- 689 [37] Hall C pion-SIDIS results, https://hallcweb.jlab.org/experiments/HALLC\_SIDIS/.
- [38] A. Bacchetta, V. Bertone, C. Bissolotti, G. Bozzi, M. Cerutti, F. Piacenza, M. Radici, and
   A. Signori, J. of High Eng. Phys. 10, 127 (2022).
- [39] A. Bacchetta, V. Bertone, C. Bissolotti, G. Bozzi, M. Cerutti, F. Delcarro, M. Radici, L. Rossi,
   and A. Signori (MAP), JHEP 08, 232 (2024), arXiv:2405.13833 [hep-ph].
- 694 [40] M. Cerutti, Private communications, 2024.
- 695 [41] P. E. Bosted and M. E. Christy, Phys. Rev. C 77, 065206 (2008).
- 696 [42] J. Agarwala et al. (COMPASS), Nucl. Phys. B **956**, 115039 (2020), arXiv:1912.10322 [hep-ex]